Global Scientific JOURNALS
GSJ: Volume 13, Issue 1, January 2025, Online: ISSN 2320-9186
www.globalscientificjournal.com

# PREPARATION, CHARACTERIZATION, AND KINETIC DEGRADATION MODELLING OF POLYIMIDE-NICKEL NANOCOMPOSITE SERIES.

Jaji Nuru-Deen[1], Othman Muhammad Bisyrul Hafi[2], Chua Yong Shen[3] & Thabit Hammam Abdurabu[4].

[1]*Post Doctoral Principal Lecturer& Researcher Fellow, Department of Chemistry, Federal College of Education Technical PMB 060 Gombe, Gombe State, Nigeria. nurudeenjaji@fcetgombe.edu.ng & School of Chemical Sciences, Universiti Sains Malaysia, Penang 11800, Malaysia*
[2]*Senior Lecturer & Research Guide, School of Chemical Sciences, Universiti Sains Malaysia, Penang 11800, Malaysia, bisyrul@usm.my*
[3]*Associate Professor & CO-Research Guide, School of Chemical Sciences, Universiti Sains Malaysia, Penang 11800, Malaysia, yschua@usm.my*
[4]*Post Doctoral Fellow & Research advisor, Interdisciplinary Research Center for Industrial Nuclear Energy King Fahd University of Petroleum & Minerals, Academic Belt Road, Dhahran 31261, Saudi Arabia, hammam.tha@gmail.com*

**Corresponding author**
*Muhammad Bisyrul Hafi Othman
Email bisyrul@usm.my



**KeyWords**

Activation energy, Characterization, Kinetic degradation, Kinetic Modelling, Nanocomposite, Nickel nanoparticles, Preparation, Polyimide.

## ABSTRACT

In situ prepared polyimide series with incorporated nickel nanoparticles were fabricated by a solution blending technique. The chemical structure of the polyimide-nickel nanocomposites was confirmed by Fourier Transform Infrared spectroscopy (FT-IR) and Proton-Nuclear Magnetic spectroscopy (H-NMR). The morphology of the polyimide-nickel series was verified by Scanning Electron microscopy (SEM). The non-isothermal kinetic behavior of the fabricated BPADA-BAPP-PINiNCs series was investigated by thermogravimetric analysis (TGA) in a nitrogen atmosphere at heating rates (β) of 5, 10, 15, 20, and 25°C/min. This study is an attempted to clarify the effects of nickel nano particles (NiNPs) on the non-isothermal degradation kinetics using Flynn–Wall–Ozawa and Kissinger models of thermal degradation analysis. The derived apparent activation energies ($E_a$) were found to fit well with each other (showing the same trend) thereby justifying the models used

for the studies. The $E_\alpha$ showed significant differences at conversion (α) > 0.7, which indicates the role of Ni loading towards degradation behavior. Based on the analysis of the results, the lifetime prediction at 5% mass loss was found to decreases in the following order: 1% > 5% > 10% directly related to the mobility of BPADA-BAPP PI backbone chain. Therefore, the presence of various nickel nanoparticle loading reveals their contributions towards thermal degradation and stability of the fabricated polyimide-nickel nanocomposites.

## INTRODUCTION

In recent decades, nanoscale inorganic materials have been broadly employed as reinforcements in polyimide matrix because of their exceptional properties. The resulting nanocomposites are extensively identified as rapidly growing areas of research interest in nanotechnology [1] Polymer-inorganic nanocomposite possesses unique properties such as thermal stability, good mechanical performance [2], and improved electrical properties [3]. Polymer-inorganic nanocomposites compared to pure polymers and micro-composites have enhanced material performance such as tensile properties, solvent resistance, and barrier properties [4]. Polymer-inorganic nanocomposites are endowed with special functionalities including bio-catalysis, optical properties, and conductivity [5]. These class of magnetic polymer-inorganic nanocomposites include polymer-iron, polymer-nickel, polymer-platinum, and polymer-cobalt nanocomposites.

Polyimides are extensively employed in thermoplastics, microelectronics, permeation sensors, adhesives, memory devices, dielectrics, and optics, as well as possessing good anti-corrosion properties [6]. Despite the industrial and technological applications of polyimides, their processing is limited by difficulties due to their high glass transition temperature and lack of solubility in most organic solvents [7]. Similarly, the applications of polyimides in industrial scale are equally limited because they lack thermal and electrical conductivity. Polyimides are non-conductive, hence the addition of inorganic material such as metal nanoparticles are necessary to offer electrical and thermal transmission [8] [9]. Nanomaterials used as fillers in polymer matrices are typically clusters of atoms with sizes ranging from 1 to 100 nm and display magnetic, electrical, and optical, properties that vary with size [10]. As these inorganic nanoparticles become uniformly intersperse within polymer matrices, they tend to exhibit exceptional characteristics that are better compared to their constituents because of hybrid and synergistic properties. Therefore, the fabricated nanocomposites can combine the properties of polyimides and inorganic nanoparticles with subsequent diversified applications [11].

Recently, various nanoparticle inorganic filler materials with a high surface area have been used to enhance the performance of polyimide matrices [12]. Okafor and Iroh [13] reported the synthesis of graphene polyimide-nickel oxide nanocomposites. They reported that, electrochemical characteristics of graphene polyimide nanocomposite sheets became enhanced when voids were created in the nanocomposites. Thereafter, nickel oxide was inserted into the composite sheets. The specific capacitance of the nickel oxide dopped composite was greatly improved in comparison to the pure graphene-polyimide composite electrode. Similarly, Yoonessi *et al* [14] prepared polyimide-nickel graphene nanocomposites by tethering nickel nanoparticles to graphene through carbon layers. The oxidation of nickel nanoparticles was prevented by covering them with a thin film of amorphous carbon. The prepared composites showed magnetic as well as excellent electrical properties. The physical properties of the composites were enhanced as the nickel nanoparticles content increased. Gao *et al* [15]. developed a highly flexible and multifunctional polyimide nickel film. They found that the nanocomposite films with conductive nickel layer exhibited adaptable thermal coefficient of resistivity on thermal treatment at various temperatures. They believed the characteristic temperature endowed the composite with great potential applications. Hence, the incorporation of nickel nanoparticles into polyimide matrix holds huge potential applications.

In this work we prepared BPADA-BAPP polyimide and subsequently incorporated nickel nanoparticles into the polyimide matrix, to produce 1 wt%, 5 wt%, and 10 wt% polyimide-nickel nanocomposites. The chemical and structural characteristics of the polyimide and nanocomposites were studied by FT-IR and H-NMR. The morphology of the composites was revealed by SEM, while the chemical composition was confirmed by EDX. The thermal properties were thoroughly investigated by TGA to obtain Ozawa and Kissinger plots used in the evaluation of activation energy. The processibility of polyimide-nickel nanocomposites was established by their solubility in common solvents as well as the degree of imidization.

## EXPERIMENTAL

### Materials

4,4'-(4,4'-isopropylidenediphenoxy) bis-(phthalic anhydride) (BPADA) (>97%) monomer, and 4,4'-(4,4'-Isopropylidenediphenyl-1,1'-diyldioxy) dianiline (BAPP) (98%) monomer, were supplied by Sigma-Aldrich product of Germany. N-Methyl-2-pyrrolidone (NMP) (99%) supplied by ACROS ORGANICS product of Netherlands, was employed as a solvent for the synthesis. NMP was further purified by reflux over calcium hydride as drying agent,

under nitrogen atmosphere. Tetrahydrofuran (THF) (99%) supplied by Merck Darmstadt Germany and used as solvent. Ultra-pure water was obtained from the analytical instrument laboratory (MUPA Lab.), School of Chemical Sciences USM. In situ synthesized Nickel nanoparticles [9]. All raw materials were utilized as received except NMP.

## Fabrication of BPADA BAPP PINiNCs Thin Film

### *Synthesis of BPADA-BAPP PI Thin Film*

1.03 g of BAPP in 25 mL of NMP were mixed in a reactor at ambient temperature at the beginning rinsed for 5 minutes with $N_2$ gas on a hot plate stirrer, stirring steadily till the mixture was homogeneous, 1.30 g of BPADA added and stirred for 2 h under nitrogen gas flow. Product washed with 100 mL of ultra-pure and for 24 hours, baked at 90 degrees Celsius. Followed by casting as well as stepwise heating at temperature of 30-50 for 1h, 50-70 for 1h, 70-100 for 1 h, 100-150 for1 h, 150-180 for 1h and cooling from 180-30 $^oC$ for 12 h (overnight). The product obtained was labelled pure BAPP-BPADA. The product 2.3218 g (99.6 %) was used in the preparation of thin films. Four thin films of pure polyimide (P-1), polyimide-nickel 1 wt% (P-2), polyimide-nickel 5 wt% (P-3) and polyimide-nickel 10 wt% (P-4) were prepared using the above procedure as summarized in **Table 1**.



### *Preparation of BPADA-BAPP PINiNCs Thin Film*

About 0.5490 g of BAPP-BPADA polyimide was dissolved in 6 mL of NMP in a reaction flask initially purged for 5 minutes with $N_2$ gas. The PI was stirred vigorously to form a homogeneous solution under nitrogen gas flow for 3 h at room temperature. Then 0.0003 g of Ni nanoparticles (1wt%) dissolved in NMP was added onto the homogeneous polyimide mixture. The mixture was further stirred for 1 h. the product was poured into a petri dish and the solvent evaporated in the following stages: 90 $^oC$ for 12 h, 120 $^oC$ for 2 h, 150 $^oC$ for 1 h, 180 $^oC$ for 1 h, 200 $^oC$ for 1 h and cooling overnight from 200 $^oC$ to room temperature. The product obtained was (BAPP-BPADA-Ni nanocomposite with 1 wt% Ni). The same procedure was used in synthesis of 5 wt% and 10 wt % BPADA-BAPP-Ni nanocomposites. The results of the synthesis are presented in **Table 1**.

**Table 1** Summary of the preparation of thin films of pure polyimide and polyimide-nickel nanocomposite series. Repeated 4, 4, 5, and 5 times respectively.

| Designation of series | Weight % Ni (g) | Weight of polyimide (g) | % Yield | Thickness of polyimide (mm) |
|---|---|---|---|---|
| BPADA-BAPP | 0 | 0.4502 | 98.0 | 0.006 |
| BPADA-BAPP/Ni 1wt% | 1 | 0.4504 | 98.0 | 0.006 |
| BPADA-BAPP/Ni 5wt% | 5 | 0.4511 | 97.9 | 0.006 |
| BPADA-BAPP/Ni 10wt% | 10 | 0.4529 | 98.0 | 0.006 |

The reaction leading to the formation of products is shown in **Figure 1**. The first stage involves the formation of polyamic acid from the monomer units by re-dissolving pure polyimide in NMP. The calculated percentage of nickel nanoparticles is then added to the polyamic acid and cured to yield polyimide- nickel nanocomposite. The nickel atoms are bonded to oxygen atoms through hydrogen bonding to form the structure shown in **Figure 1**.

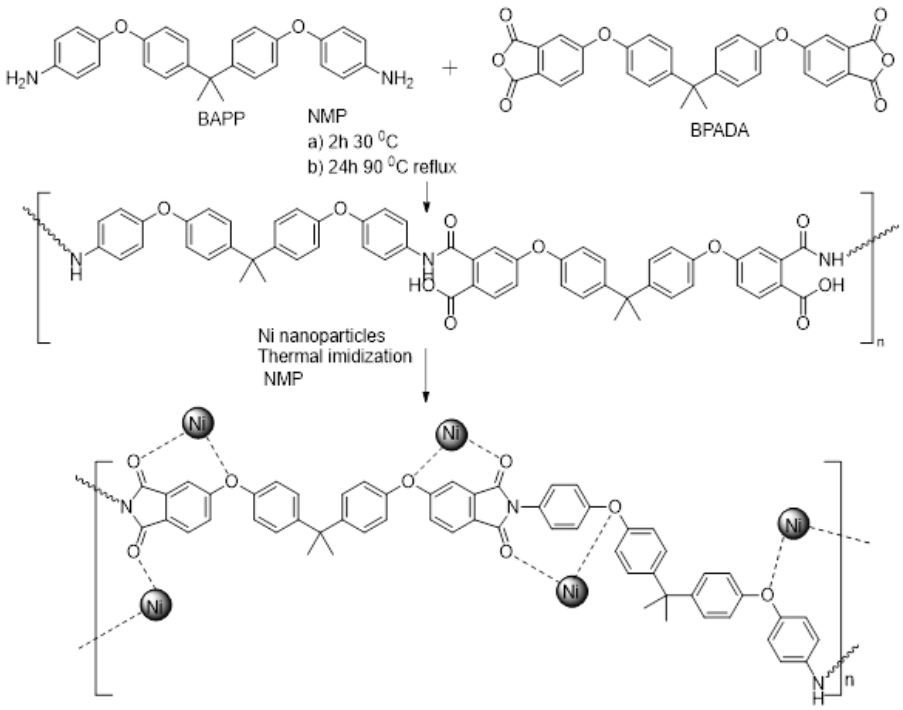


**Figure 1** Synthesis of Polyimide /Ni nanocomposite.

## Characterization

The Proton-nuclear magnetic resonance (1H-NMR) spectra were obtained with a Bruker 500 Ultra Shield TM Model at an operating temperature of 40 ℃ and frequency of 500 MHz using deuterated chloroform ($CDCl_3$-d1) as solvent to confirm the final structure. Into 0.6 milliliters of chloroform-d ($CDCl_3$) was dissolved about 10 milligrams of the sample and placed in NMR test tube. Fourier Transform Infrared Spectra (FT-IR) was recorded on PerkinElmer spotlight (ATR-FTIR) 2000 FT-NIR spectrometer operating in diffuse reflectance mode. Samples were exposed to 32 scans and the spectra acquired at a resolution of 4 $cm^{-1}$ in the range of 4000 - 600 $cm^{-1}$. X-ray powder diffraction (XRD) was used to determine the structure and phase composition of the synthesized NiNPs using advanced X-ray diffractometer (Germany) with Cu Kα (λ = 1.54178 Å) X-ray radiation source and a sodium iodide scintillation type detector at ≤ 10 ° ≥ 80 °. Field Emission Electron Microscope (FESEM model NOVA NANOSEM 450 10 kV), equipped with Energy Dispersive spectroscopy (EDX-SEM) was employed to determine the morphology such as shape, size, and Ni nanomaterial distribution into the polyimide matrix, while the EDX was used to determine the various elements in the prepared composites. Before loading on SEM chamber, the PI films were cut into 10 x 10 mm dimension and attached to the aluminum sample holders with carbon double sided tape. The samples were observed in the magnification of 2.5 KX, 5 KX, and 10 KX. Thermalgravimetric analysis (TGA) was performed using an STA 6000 Thermogravimetric analyzer (Perkin Elmer). The samples were tested under an $N_2$ gas flow with a heating rate of 20 $^oC\ min^{-1}$ in the temperature range of 30-800 $^oC$.



## RESULTS AND DISCUSSION

### Preparation consideration of polyimide-nickel nanocomposite

Solvent-polyamic acid interaction constitute the dominant determinants of polyimide films properties, the degree of imidization so also the attendant by-products like the formation of transformable anhydride. The polyamic acid-solvent interplay involves hydrogen bonding resulting in the production of polyamic acid-solvent complex. Once the polyamic acid-solvent complex is dissociated, the unreacted molecules of the solvent aid the polyamic acid film's plasticization. Thereby facilitating imidization as it can only happen after the complex is dissociated. The degree of imidization has considerable effect on the performance of any polyimide.

#### *Imidization degree determination*

The degree of imidization the polyimide formed by the reaction of BPADA and BAPP is the ratio of number of imidized groups to the number of all imidizable groups as in **Equation 1**.

$$\text{Imidization degree} = \frac{Number\ of\ imidized\ groups}{Total\ number\ of imidizable\ groups} * 100 = \frac{n_i}{n_a} * 100 \qquad \textbf{Equation 1}$$

Where $n_a$ is the number of imidizable groups and $n_i$ is the number of imide groups. The imidization degree was calculated in accordance with Lambert-Beer law. The C-N stretch in the aromatic imide ring at 1380 $cm^{-1}$ was selected as the reference for the imidized group, while the C-C stretch of *p*-substituted benzene with absorption peak at 1500 cm-1 was chosen as the internal standard. The FT-IR of the polyimide at various temperatures of imidization as it was heated from 25, 50, 70, 100, 150, and 180 $^oC$ are presented in **Figure 2**. The disappearance of the amide group at 3400 $cm^{-1}$ and the carbonyl group at 2900 $cm^{-1}$ at the temperature of 180 $^oC$, confirms the complete conversion of the polyamic acid of the precursor to the polyimide of the product.

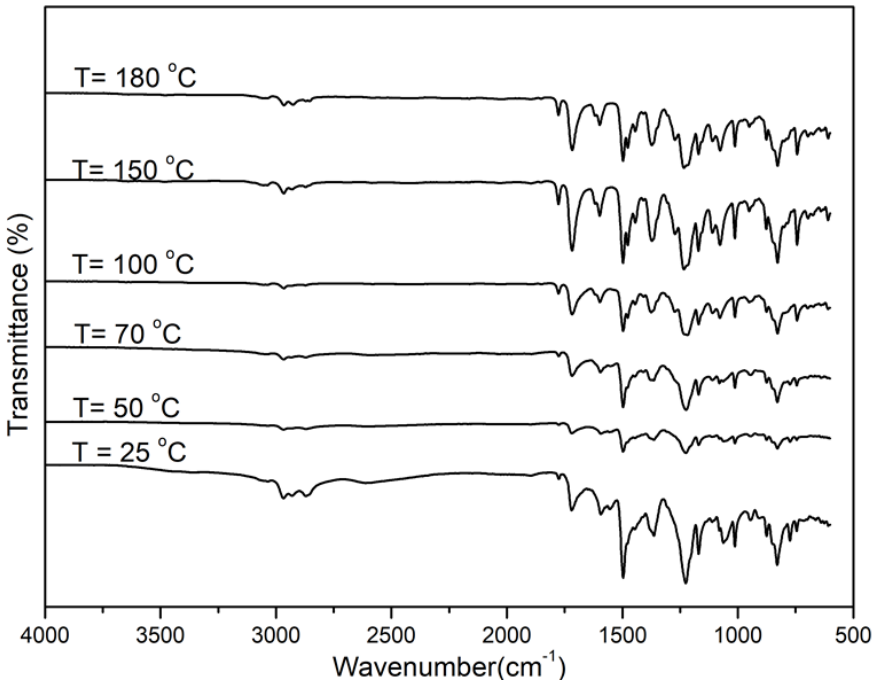


**Figure 2** FT-IR of polyimide at various temperatures of imidization. Repeated 3 times.

The degree of imidization plot in **Figure 2** shows that at 100 $^oC$ less than 30% of the polyimide film had undergone imidization. Whereas at 120 $^oC$ less than 40% was imidized. The peak at around1120 $cm^{-1}$ is attributed to the absorption of an imide group ($(CO)_2NC$) which is relatively weak. This is due to the conversion of some of the cured polyamic acid to intermolecular links [16]. Due to low concentration of imide group, there are few imide chains

and as such no peak splitting was observed 11500 ~ 1700 $cm^{-1}$ as well as 1100 ~ 1300 $cm^{-1}$ which are attributed to the absorption band of the C=O imide group. The absorption bands of PI are1774 and 1727 $cm^{-1}$ for C=O asymmetrical and symmetrical stretching respectively [17]. The plot of degree of imidization against temperature is shown in **Figure 3.**

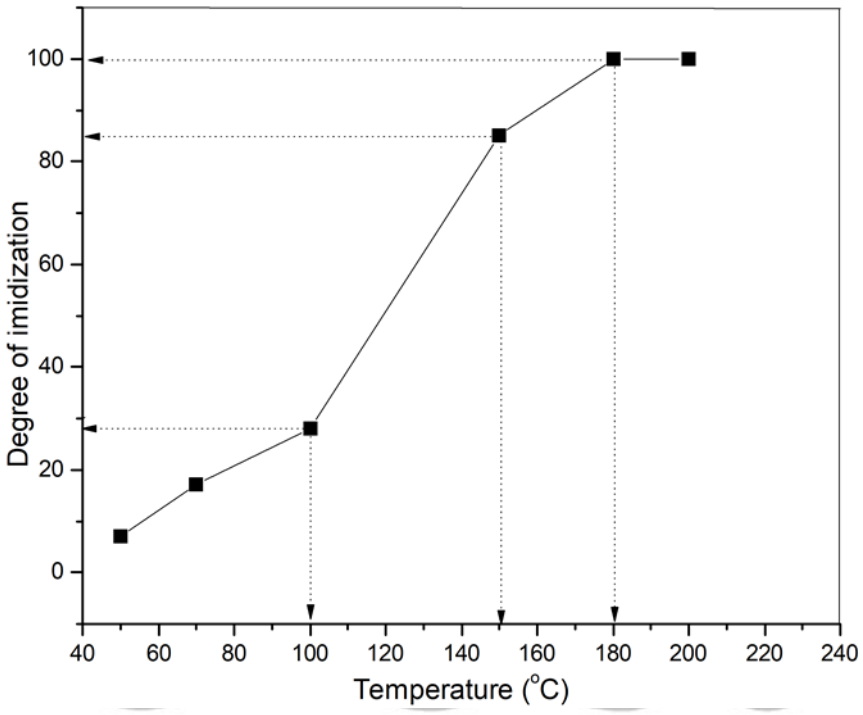


**Figure 3**: Degree of imidization of pure polyimide. Repeated 4 times.

The plot reveals the complete imidization of the BPADA-BAPP polyimide at 180 °C and the degree of imidization is about 85% at 150 °C. The thin film of BPADA-BAPP polyimide was fully imidized at 180 °C. The peak at 1725 $cm^{-1}$and 1774 $cm^{-1}$ became more pronounced, these results agree with [18]. The stepwise thermal curing of the polyamic acid resulted in 100% imidization at 180 °C. The thermal imidization did not affect the -$C(CH_3)_2$ and C-O-C the main chain of the characteristic backbone of the polyimide. The solution mixing fabrication of BPADA-BAPP polyimide is exothermic hence, there is high probability of intermolecular links resulting in low intensities of the imide group.

***Chemical structure confirmation***

The FT-IR spectroscopic plots for pure polyimide (P-1), 1wt% PI-Ni (P-2), 5 wt% PI-Ni (P-3), and 10 wt% PI-Ni (P-4) are presented in the **Figure 3.**

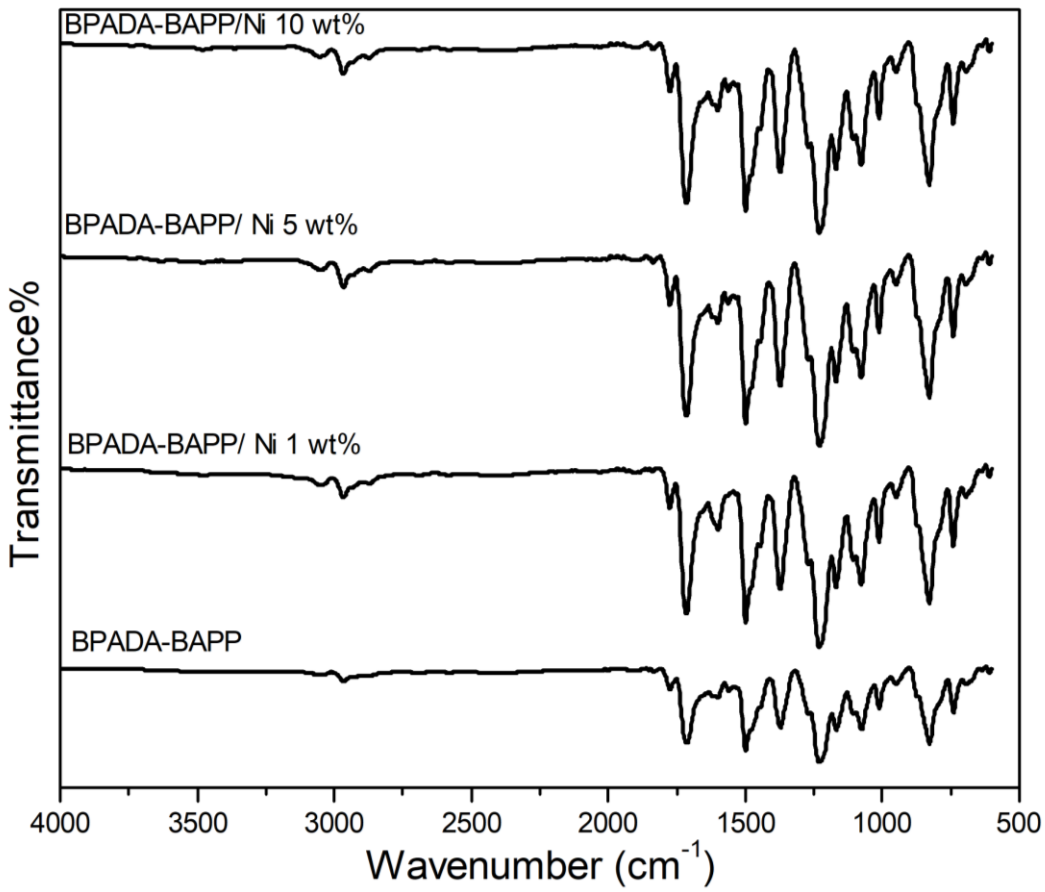


**Figure 4** FT-IR plots for pure polyimide, PI-Ni1wt%, PI-Ni 5 wt% and PI-Ni10 wt%. Repeated 4, 5, and 5 times respectively.

The chemical structure of the pure polyimide (P-1) and PI-Ni series (P-2, P-3, and P-4) were characterized by FT-IR analytical technique. The FT-IR was conducted to confirm the imidization of the pure polyimide and the polyimide/nickel series. The FT-IR spectra in **Figure 4** shows the characteristic C=O in imide ring absorption band at 1777 $cm^{-1}$ asymmetric stretching vibration, 1718 $cm^{-1}$ corresponding to imide C=O symmetric stretching vibration. The absorption band at 741$cm^{-1}$correspond to imide ring deformation. The C-N in imide ring were observed at about 1370 – 1374 $cm^{-1}$ stretching vibration, whereas the C=O in CO-NH characteristic band appeared at 1600 $cm^{-1}$ confirming the imidization of the pure polyimide and the polyimide/nickel series [19]. The removal of $H_2O$, $CO_2$, CO,

and hydrocarbons during imidization produces strong absorption peak of hydrocarbon at 2968 $cm^{-1}$. This peak increases with increasing nickel content. The nickel nanoparticles serve as flashpoints supplying heat to the surrounding polyimide matrix. Similarly, the polyimides show peaks at 1712 - 1772 $cm^{-1}$ attributed to the symmetrical carbonyl (C=O) stretch vibrations. These peaks increased as the nickel nanoparticle weight percent is increased from 1 to 5 and then 10 wt%. The peaks at 1712 $cm^{-1}$ (-CO stretch) 1229 $cm^{-1}$ (-C(CO)O-stretch) and 1092 $cm^{-1}$ (-OCC-stretch) are characteristic of polyimide and are clearly seen in the pure polyimide in **Figure 4**, with increasing intensity in the polyimide nanocomposites [20].

## Structural conformation of pure polyimide

The synthesized polyimide structure was investigated using H-NMR. **Figure.5** presents the H-NMR of pure polyimide.

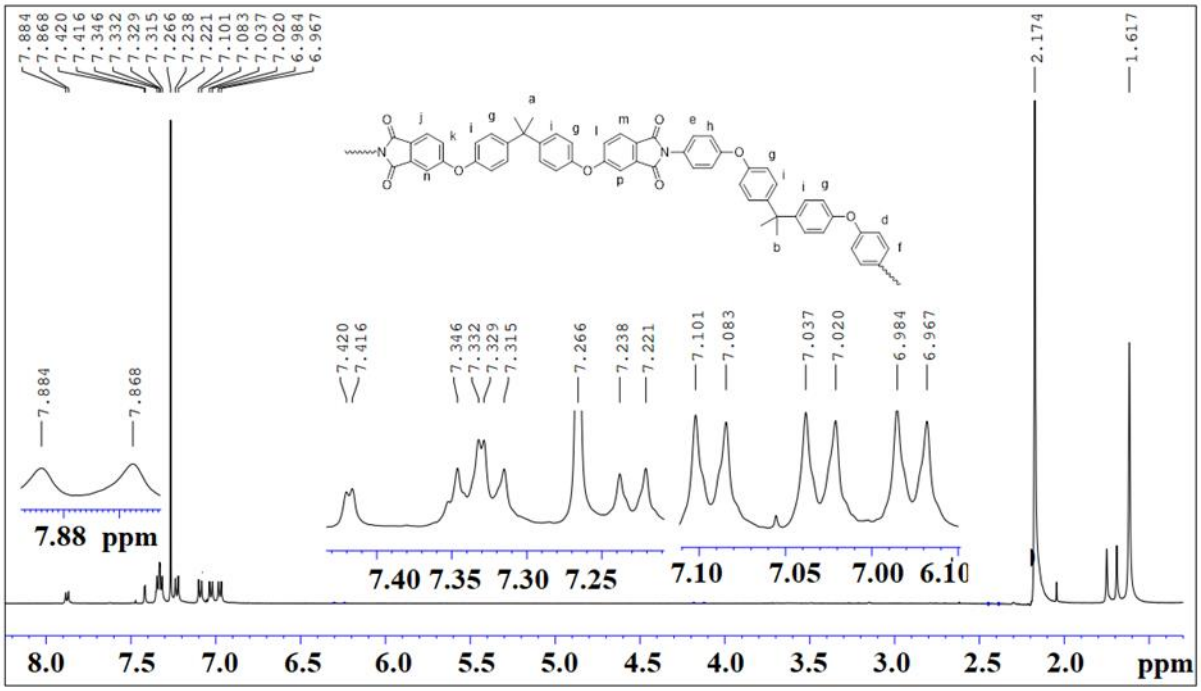


**Figure 5** H-NMR OF BPADA-BAPP. Repeated 3 times.

The signal of residue $CHCl_3$ in the spectra indicate that $CDCl_3$, $CHCl_3$ and trimethyl silane the solvents used were not 100% deuterated. $CDCl_3$ was used with 99.99% atom D and the rest was the excess $CHCl_3$ and trimethyl silane (TMS) as the references. Both $CHCl_3$ and TMS were interpreted as singlets in **Figure 5** of the $^1$H-NMR spectra. The signals corresponding to the BPADA-BAPP (P-1) main chain can be clearly identified from the spectra. The signals

between 1.00 ~ 7.88 ppm are assigned to $^1$Hj, $^1$Hk, $^1$Hp, $^1$Hm, and $^1$Ha which corresponded to the proton from BPADA and BAPP. The $^1$Ha is assigned to the methyl group (-$CH_3$) from BPADA monomers which appeared at range 1.64 ~ 2.17 ppm as singlet due to the absence of protons on the adjacent carbons. The $^1$Hb, $^1$Hc, $^1$Hd, $^1$He and $^1$Hf are from BPADA monomer while $^1$Hh, $^1$He, $^1$Hg, $^1$Hi, $^1$Hb, $^1$Hd, and $^1$Hf are from BAPP monomer. All signals indicated an aromatic ring at 6.93-7.88 ppm and appeared as doublet except for $^1$Hf which is represented as singlet. The results presented in **Figure 5** indicates that the P-1 was successfully prepared.

### Solubility studies of PI and PI/Ni series in common solvents at room temperature

Chemical solubility enables the determination of resistivity of the samples as well as the processability of the pure PI and PI/Ni series of nanocomposite thin films in protic, polar protic, non-polar and non-polar protic solvents. The results obtained are presented in **Table 2.**

**Table 2**: solubility of pure PI and PI/Ni nanocomposites. Repeated 3 times.

| Solvent | Solubility | | | | Classification of solvent |
|---|---|---|---|---|---|
| | Pure PI (P-1) | PI/Ag 1wt% (P-2) | PI/Ag 5wt% (P-3) | PI/Ag 10wt% (P-4) | |
| $H_2SO_4$ | + | + | + | + | Protic |
| HCl | - | - | - | - | Protic |
| HF | - | - | - | - | Protic |
| KOH | - | - | - | - | Protic |
| $NH_4OH$ | - | - | - | - | Protic |
| NMP | + | + | + | + | Polar protic |
| DMF | + | + | + | + | Polar protic |
| DMSO | - | - | - | - | Polar protic |
| THF | + | + | + | + | Polar protic |
| $H_2O$ | - | - | - | - | Polar protic |
| $CH_3OH$ | - | - | - | - | Polar protic |
| Acetone | - | - | - | - | Polar protic |
| Chloroform | + | + | + | + | Polar protic |

| | | | | | |
|---|---|---|---|---|---|
| Hexane | - | - | - | - | Non-Polar protic |
| Benzene | - | - | - | - | Non-Polar |

+ = soluble and - = insoluble

The prepared polyimides namely P-1, P-2, P-3, and P-4 showed good solubility in polar aprotic solvents such as NMP, DMF, THF, and chloroform at ambient temperature. The sample polyimides exhibit low solubility in hexane and benzene due to low dielectric constant of these solvents. The excellent solubility in polar protic solvents can be attributed to the introduction of the bulky pendant triphenyl imidazole group into the polymer backbone. The bulky pendant triphenyl group reduced the packing force as well as the interchain interactions leading to better diffusion of solvent molecules [21]. Similarly, polarizability from ether linkages and imidazole ring in the backbone served to improve their solubility in the organic solvents. Consequently, all the prepared polyimides can be processed from solution. The obtained polyimide films by solution casting were flexible and tough. The films are transparent with light yellow color [22].

### 3.4. X-ray diffraction analysis

X-ray spectroscopy was conducted to determine the amorphous nature and crystallinity of the synthesized pure polyimide and polyimide-nickel nanocomposite series. The X-RD diffractions of polyimide and polyimide composites are presented in **Figure 6**.

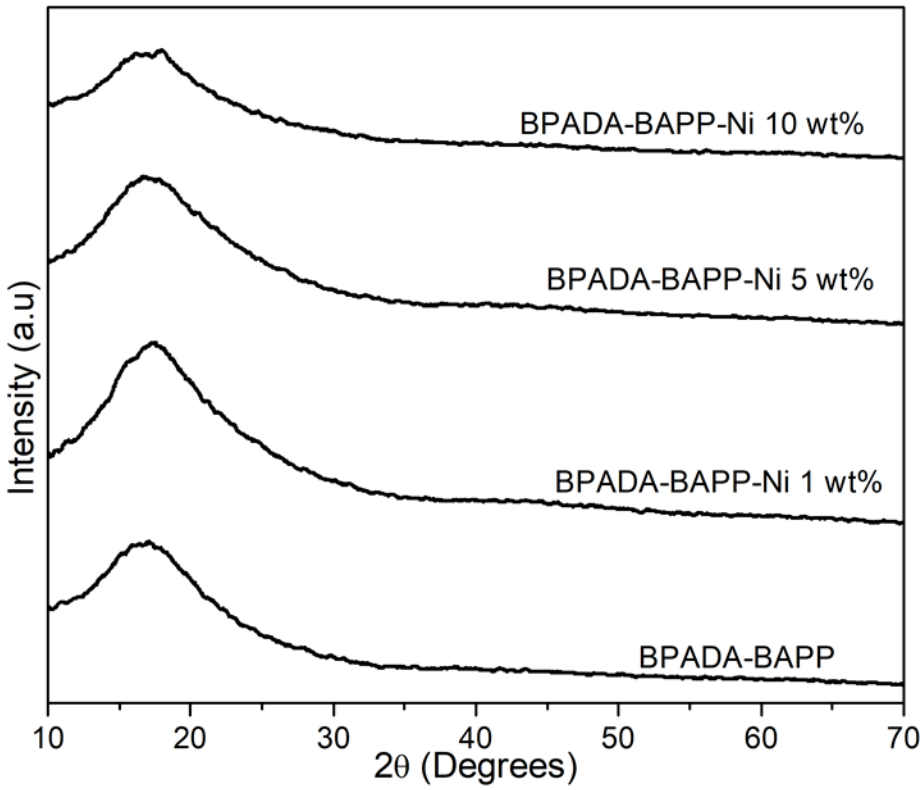


**Figure 6 XRD** Pattern of pure polyimide and polyimide-nickel nanocomposites. Repeated 3 times.



The XRD pattern reveals a broad peak in the range 2 theta at 10 ~ 20°. This peak is attributed to the polyimide matrix, indicating that the polyimide is amorphous. The pattern shows no sharp peaks, suggesting that all the PI series are amorphous. There are no sharp peaks to suggest crystalline pattern despite the introduction of NiNPs into BPADA-BAPP matrix. The low degree of crystallinity is due to the low Ni filler loading content in the nanocomposites of 1%, 5% and 10% in P-2, P-3, and P-4 respectively. This result agreed with [14] in which amorphous polyimide did not show any sharp peaks in the XRD.

**Field Emission Scanning Electron Microscopy (FESEM) equipped with Energy Dispersive X-ray (EDX) Spectroscopy**

FESEM was employed to perform the Morphological analysis of the polyimide samples and examine the possible phase separation occurring between BPADA-BAPP PI and Ni filler nanomaterial. The concentration of Ni was set at 1 wt%, followed by 5 wt% and finally, 10 wt%. Blending of Ni loads into the BPADA-BAPP PI matrix resulting in the phase separation of BPADA-BAPP PI matrix and Ni. The SEM micrographs of BPADA-BAPP PI series are shown in **Figure 7 a, b, c** and **d** obtained at magnification, 2.5 kX. The figure shows the morphology of the interaction between

the PI and nickel nanoparticles in the thin polyimide film. The nanoparticles are well attached within the polyimide matrix indicating a good interfacial bonding of the conductive nanocomposite film [15]. The Ni nanoparticles were homogenously dispersed throughout the BPADA-BAPP PI matrix for the P-2 fabrication (**Figure 7b)** showing the phase separation between them due to attraction of Ni to the BPADA-BAPP parent chain through hydrogen bonding. At thermal imidization, the hydroxyl bonds were broken to form the PI. The Ni nanoparticles are then attracted to the main chain of BPADA-BAPP PI. It then encounters the BPADA-BAPP PI chain packing. This results in the enhancement of the free volume owing to disturbance in dense chain packing of BPADA-BAPP polyimide.

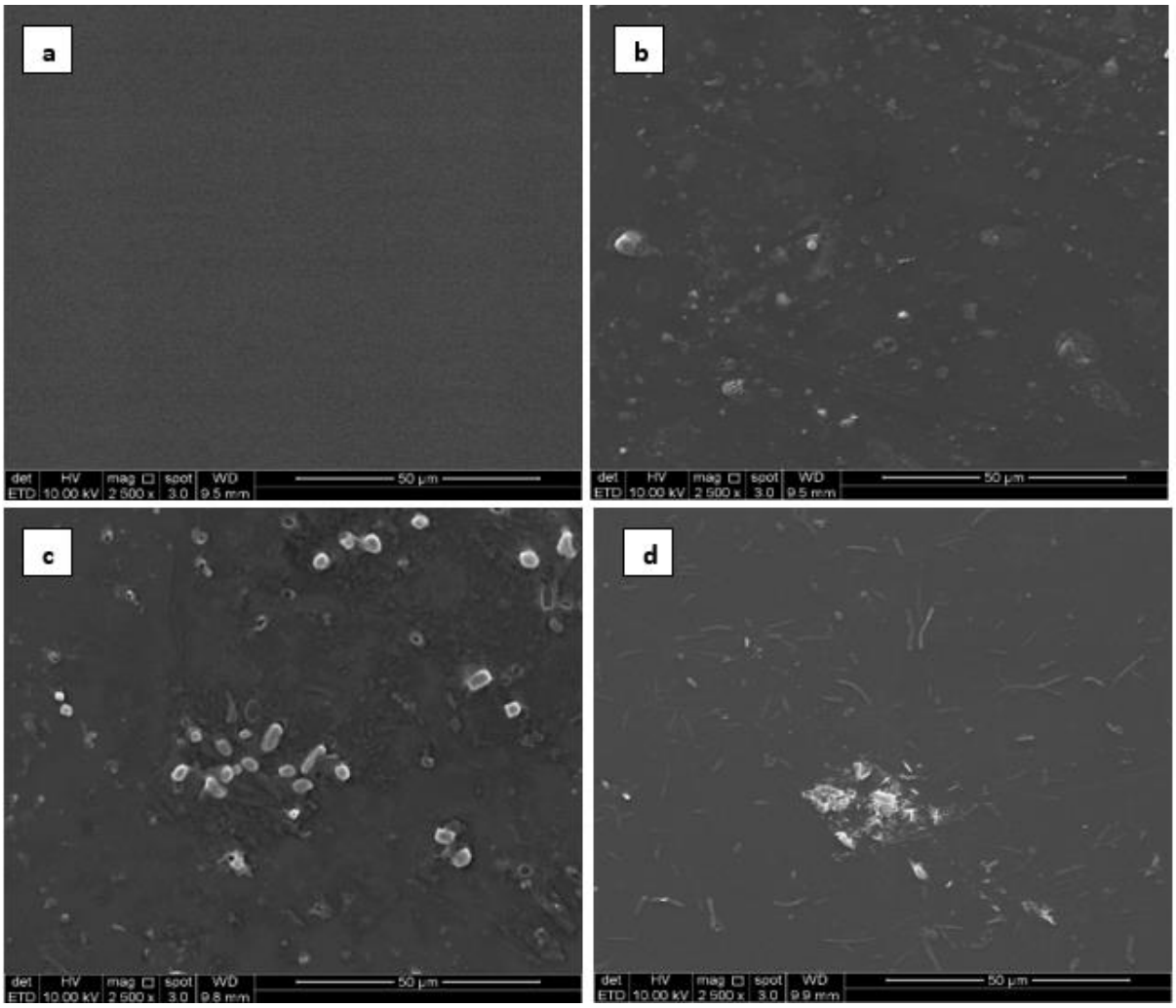


**Figure 7** SEM monograms of (a) PI, (b) PI-Ni 1wt%, (c) PI-Ni 5 wt% and (d) PI-Ni 10wt%.

Repeated 5 times in each case.

Therefore, the free volume increased as phase separation between BPADA-BAPP PI matrix and Ni were formed. Interestingly, incorporating Ni into BPADA-BAPP PI matrix after conventional two-steps method (P-2, P-3 and P-4) expectedly increased the free volume due to the disturbed dense packing of BPADA-BAPP PI chain.

In addition, the Ni nanoparticles made some areas of parent chain loosened during chain arrangement and forced it to increase the free volume of BPADA-BAPP PI matrix. After thermal imidization, the loosened chain area became compressed and formed a curve on the P-4 phase as shown in **Figure 7d**, the observed strong interfacial adhesion in the Ni and BPADA-BAPP composite superstructure, originates from the strong interaction between Ni and characteristic organic groups for instance C-O-C and C=O of the PI matrix leading to hydrogen bonding. Particle agglomeration as observed in P-3 and P-4 occurred due to the high concentration of Ni nanoparticles in the PI films of P-3 and P-4, during film formation. The surface of the pure PI and polyimide nanocomposites was discovered to be free from roughness and irregularities. As the filler content increases, the agglomerate size grows, creating a competition in the energizing aspect of the Ni nanoparticles and Ni load.

There are no visible voids between the PI matrix and the Ni filler in the SEM micrographs in Figure 7(a-d), indicating that the polymer melt, bonded well with the Ni filler. As a result, the state of dispersion in the specimens indicates that Ni has a good interaction with the polymer matrix. The surface of nanocomposites becomes rougher as the diameter size increases, as micro-voids can be seen due to Ni aggregates of larger diameter size, as shown in Figure 7 (d) [23]. The non-homogeneous distribution of the nanomaterials across the membrane is one of the issues identified in the PI-Ni nanocomposite. Even though Ni nanofillers have good compatibility and adhesion with the polymer phase, specific sites of nanofillers in the PI matrix tend to form large agglomerates [24].

**Energy dispersive X-ray spectroscopic analysis (EDX)**

EDX analysis was run to investigate the elemental composition of BPADA-BDAF PIs series, to verify the presence of Ni in the BPADA-BAPP PI-NiNCs are shown in **Figure 8**. The EDX analysis of the PI series, showed elemental carbon, oxygen and Ni elements having significant presence in the BPADA-BAPP PI series, with minute nitrogen element in the pure PI. There is no phase separation shown on the surface indicates that the surface of BPADA-BAPP Pure PI is homogenous with no nickel nanoparticle. The peak for elemental carbon has the greatest intensity, while the peak for element fluorine has the least peak.

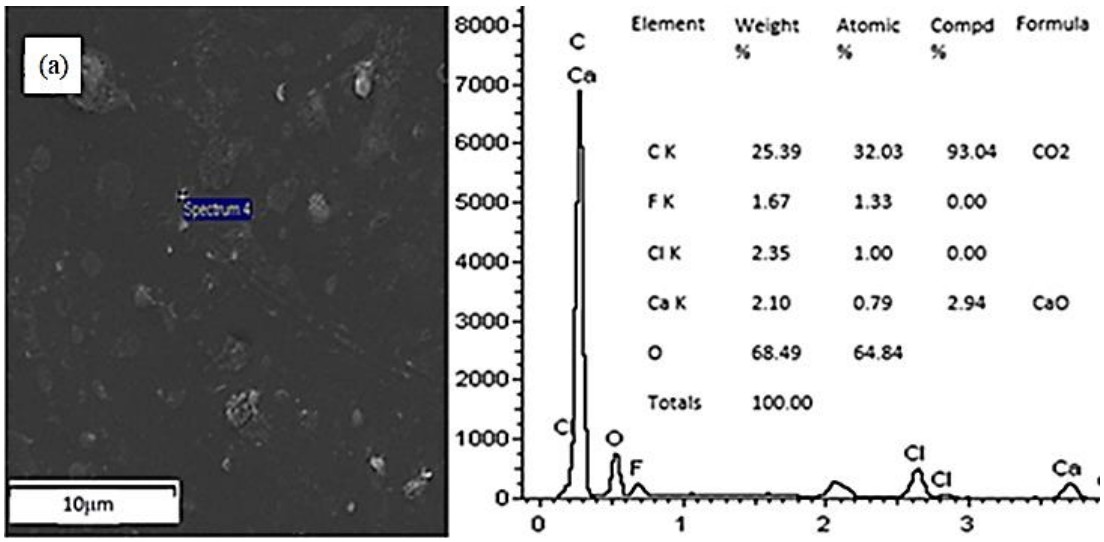
(a)
Spectrum 4
10µm
Element Weight % Atomic % Compd % Formula
C K 25.39 32.03 93.04 CO2
F K 1.67 1.33 0.00
Cl K 2.35 1.00 0.00
Ca K 2.10 0.79 2.94 CaO
O 68.49 64.84
Totals 100.00
C
Ca
O
F
Cl
Cl
Ca

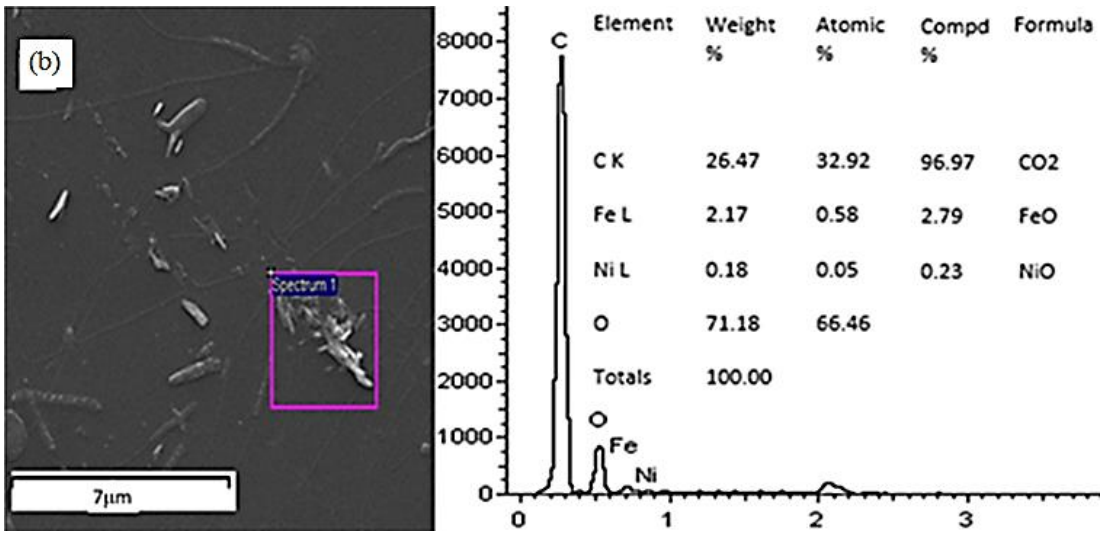
(b)
Spectrum 1
7µm
Element Weight % Atomic % Compd % Formula
C K 26.47 32.92 96.97 CO2
Fe L 2.17 0.58 2.79 FeO
Ni L 0.18 0.05 0.23 NiO
O 71.18 66.46
Totals 100.00
C
O
Fe
Ni

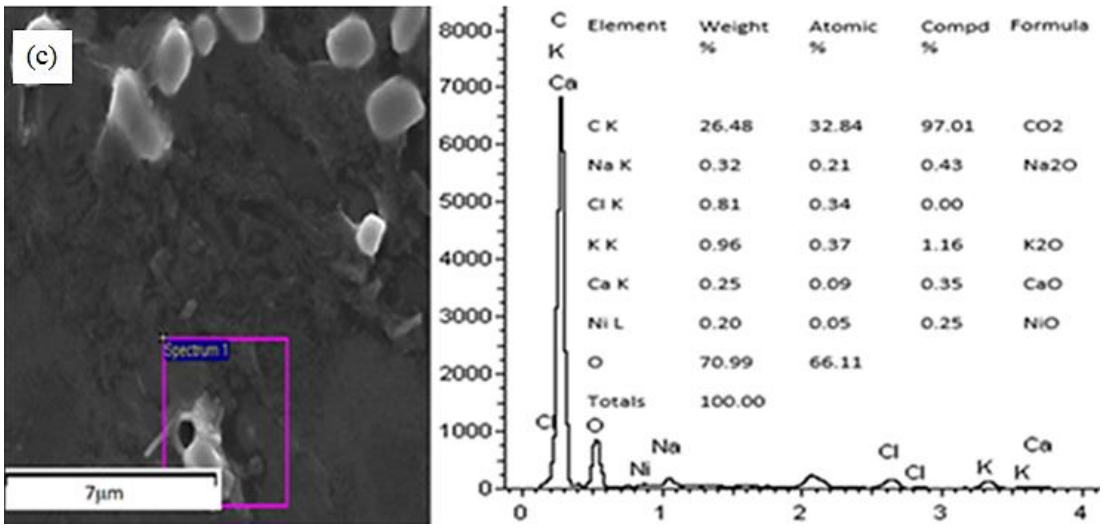
(c)
Spectrum 1
7µm
Element Weight % Atomic % Compd % Formula
C K 26.48 32.84 97.01 CO2
Na K 0.32 0.21 0.43 Na2O
Cl K 0.81 0.34 0.00
K K 0.96 0.37 1.16 K2O
Ca K 0.25 0.09 0.35 CaO
Ni L 0.20 0.05 0.25 NiO
O 70.99 66.11
Totals 100.00
C
K
Ca
Cl
O
Na
Ni
Cl
Cl
K
K
Ca

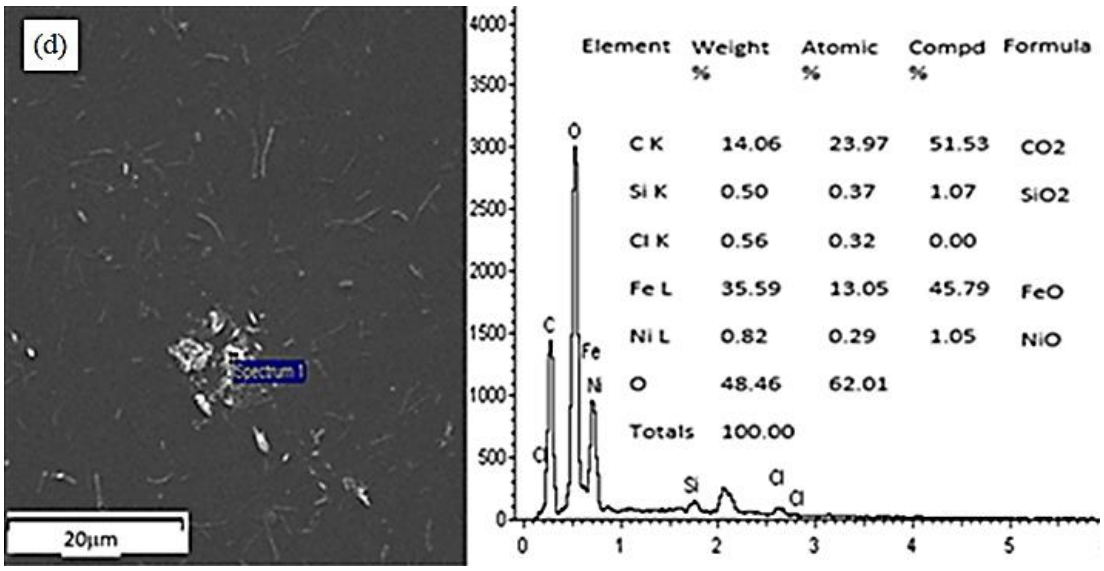


**Figure 8** SEM and EDX of (a) PI, 0 wt% (b) PI-Ni 1 wt%, (c) PI-Ni 5wt% and (d) PI-Ni 10 wt% Nanocomposite series. Repeated 5 times in each case.

Pure polyimides show no features in SEM analysis [25]. EDX investigation indicated a self-assembly of Ni nanoparticles concurrently directed on a monolayer of the PI film through chemical and physical rearrangements. The incorporation of Ni into BPADA-BAPP PI matrix was verified by the presence of Ni metal as shown in the **Figure 8 (b)**, **(c)** and **(d).** Due to the 1 wt% ratio of Ni in P-2 the Ni peak is not prominent in the EDX. However, the peak becomes more prominent in P-3 and P-4 when Ni content was raised to 5 wt% and 10 wt% Ni respectively. Therefore, more Ni was detected at higher filler loading in agreement with [26].

when 10 wt.% nickel nanoparticles are added, SEM images for the samples show nickel nanoparticles dispersed homogeneously in the polyimide matrix as shown in **Figure 8 (d)**. The nickel element observed in EDX increase to 1.05%. The larger surface area of the NiNPs may be due to aggregation of the smaller particles caused by the dissolution and precipitation processes, or to their interaction with beams of electrons during SEM measurement, which causes heat to be released.

The enhancement in the free volume due to disturbance of the dense chain packing BPADA-BAPP PI. The NiNPs caused the BPADA-BAPP PI thin film force to increase by disturbing the parent chain area in the free volume zone [27]. The intensity shown in the EDX spectrum can be used to further confirm the content of NiNPs existence

in the polyimide matrix [28]. This result suggests that there are synergistic effects in BPADA-BAPP polyimide and NiNPs [29].

## Thermogravimetric analysis

Thermogravimetric analysis (TGA) investigation was carried out to confirm changes in the thermal properties of pure polyimide matrix with the introduction of nickel nanoparticles and was presented in **Figure 9**. The TGA curve show no weight loss below 200 $^{o}$C therefore, there are no -OH groups remaining in the polyimide films of BPADA-BAPP series after the imidization process. Consequently, it is concluded that the polyimide films have undergone complete imidization.

The thermal degradation of the films displays two decomposition stages. The initial decomposition (T1) was from 200 ~ 400 $^{o}$C. This is most likely due to the breakdown of flexible segments within propylidene ($C(CH_3)_2$) bridge. which is the weakest linkage along the BPADA-BAPP polyimide backbone. The second decomposition stage (T2) began at 500 ~ 800 $^{o}$C attributed to the breakdown of heterocyclic structure or aromatic imide groups characteristically present in polyimides.



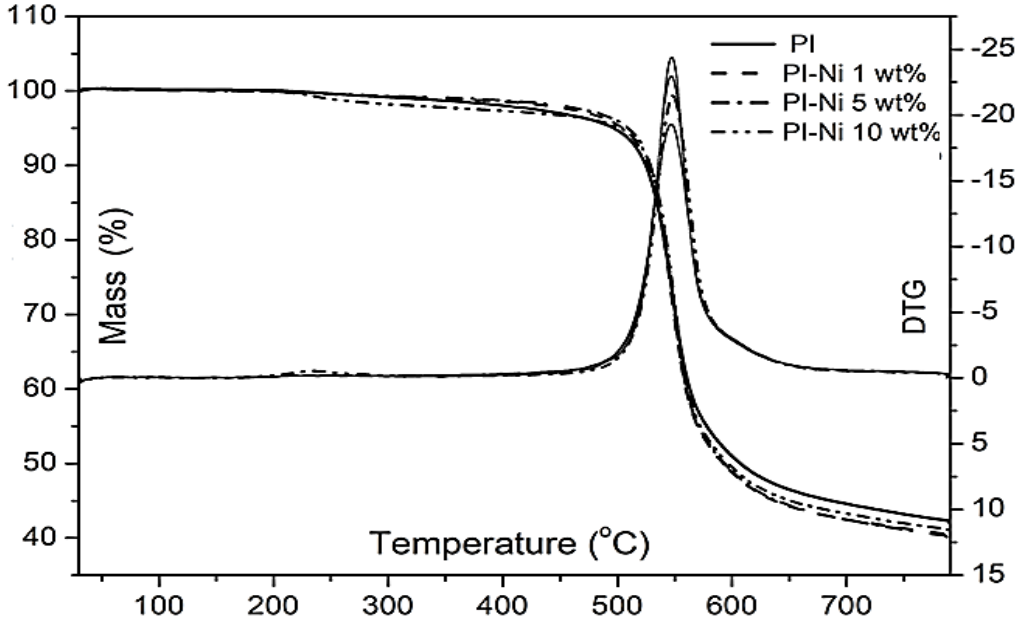


**Figure 9** TGA and DTG of PI nanocomposite series. Repeated 3 times.

The TGA curves indicate that mass loss over temperature range from 30 ~ 800 $^{o}$C is more than 56 % after the degradation completed at 800 $^{o}$C. The curves reveal that in the pure polyimide and polyimide-nickel nanocomposites, the organic functional groups such as CO, $CO_2$ and propylidene were decomposed at 200 ~ 500 $^{o}$C. It was equally noted that the slope of the curves after 650 $^{o}$C were approximately uniform. The temperature of maximum degradation ($T_{max}$) of pure polyimide was 529 $^{o}$C and 533, 535 and 528 $^{o}$C for 1 wt%, 5 wt%, and 10 wt% Ni composite films respectively. The slight increase in $T_{max}$ is attributed to low percentage of nickel filler in the polyimide nanocomposites.

The pure polyimide shows residue above 45% when degradation process completed at 800 $^{o}$C. Whereas the polyimide-nickel series had less than 45% residue at the completion of degradation at 800 $^{o}$C. The DTG curves of the Pure PI and PI-NiNCs with various loadings of NiNPs The samples revealed a single peak, attributed to the polyimide's single step decomposition process.

As a result of the increase in thermal lag, the TGA and DTG profiles shifted toward higher temperatures. The thermal degradation reactions cause the increase in the peak temperature for the maximum degradation rate with increasing heating rates due to the internal thermal gradient in the TGA crucible. The polymer and polymer nanocomposites degrade in a single step, whereas the predominant crack occurs in a limited temperature range [30]. Similarly, reported are DTG curves for BPADA-BAPP polyimide indicating a single stage degradation process [31].

The derivative weight loss DTG curves of pure polyimide and polyimide-nickel nanocomposite series are presented in **Figure 9**. The DTG plots show temperatures at which maximum weight loss occurred. The curves reveal maximum weight loss at average temperature of 529, 533,535 and 5528 $^{o}$C for pure polyimide, 1 wt%, 5 wt%, and 10 wt% Ni respectively. The DTG curves indicate a maximum weight loss temperature range of 7 $^{o}$C. The results show that the presence of NiNPs in the polyimide matrix did not alter the thermal properties of the polyimide significantly due to low filler content. The polyimide thermal characteristics of pure and PI-NiNCs are summarized in **Table 2**. The table shows thermal parameters by TGA performed in $N_2$ atmosphere at heating rate of 20 $^{o}$C min$^{-1}$. The thermal stability of the nanocomposites was investigated and supported by the analysis of pure polyimide, 1 wt% , 5 wt%, and 10 wt% Ni respectively.

**Table 2** TGA properties of pure PI and PI-NiNCs in $N_2$ gas atmosphere. Repeated 3 times in each case.

| Sample Designation | B | Char residue [a] | $T_{5\%}$ [°C][e] | $T_{10\%}$ [°C][f] | $T_{onset}$ [°C][b] | $T_{max}$ [°C][c] | $T_{end}$ [°C][d] | ΔT [°C][g] |
|---|---|---|---|---|---|---|---|---|
| Pure PI | 5 | 45.62 | 465.59 | 476.03 | 390.23 | 508.75 | 642.23 | 252.00 |
| | 10 | 45.08 | 470.07 | 490.97 | 402.02 | 520.69 | 652.62 | 250.60 |
| | 15 | 45.81 | 482.40 | 501.04 | 419.51 | 531.15 | 657.71 | 238.20 |
| | 20 | 49.16 | 486.90 | 507.41 | 423.01 | 540.92 | 673.86 | 250.85 |
| | 25 | 47.10 | 498.63 | 516.34 | 439.22 | 545.37 | 687.98 | 248.76 |
| | Average | 46.55 | 480.72 | 498.36 | 414.80 | 529.38 | 662.88 | 248.08 |
| PI-Ni 1wt% | 5 | 39.87 | 463.48 | 484.26 | 385.43 | 510.88 | 616.8 | 231.37 |
| | 10 | 37.95 | 477.82 | 499.45 | 394.06 | 527.78 | 666.32 | 272.26 |
| | 15 | 39.32 | 491.82 | 510.28 | 399.14 | 536.56 | 678.93 | 279.79 |
| | 20 | 39.48 | 496.61 | 515.11 | 423.66 | 543.41 | 663.69 | 240.03 |
| | 25 | 39.80 | 509.15 | 524.56 | 448.99 | 550.68 | 682.69 | 233.70 |
| | Average | 39.28 | 487.78 | 506.73 | 410.26 | 533.86 | 661.69 | 251.43 |
| PI-Ni 5wt% | 5 | 45.54 | 458.76 | 481.74 | 378.01 | 512.68 | 656.39 | 278.38 |
| | 10 | 37.43 | 475.37 | 499.06 | 397.91 | 528.42 | 658.38 | 260.47 |
| | 15 | 33.22 | 476.93 | 504.89 | 403.35 | 538.77 | 663.03 | 259.68 |
| | 20 | 40.05 | 501.98 | 518.98 | 422.91 | 545.44 | 665.68 | 242.77 |
| | 25 | 40.28 | 504.46 | 504.46 | 424.74 | 552.16 | 688.66 | 263.92 |
| | Average | 39.30 | 483.50 | 501.83 | 405.38 | 535.49 | 666.43 | 261.04 |
| PI-Ni 10wt% | 5 | 45.96 | 435.49 | 463.49 | 352.4 | 504.35 | 659.49 | 307.09 |
| | 10 | 45.72 | 459.80 | 484.43 | 383.66 | 519.5 | 660.37 | 276.71 |
| | 15 | 47.01 | 467.18 | 494.22 | 392.06 | 532.89 | 664.77 | 272.71 |
| | 20 | 44.24 | 478.77 | 503.28 | 402.25 | 540.22 | 676.68 | 274.43 |
| | 25 | 46.71 | 484.27 | 507.91 | 404.17 | 544.46 | 676.94 | 272.77 |
| | Average | 45.93 | 465.10 | 490.67 | 386.91 | 528.28 | 667.65 | 280.74 |

Where, [a] wt% residue at 800°C, [b] Onset temperature of degradation, [c] Temperature maximum rate of weight loss, [d] End temperature of the degradation, [e] Temperature corresponding to 5% weight loss, [f] Temperature corresponding to 10% weight loss, [g] $\Delta T = T_{end} - T_{onset}$.

The average $T_{onset}$ for the degradation of pure polyimide was 414 °C, while, for 1 wt%, 5 wt%, and 10 wt% Ni were 410, 405, and 386 °C respectively. The slight increase in $T_{onset}$ is due to Ni nanoparticles present in the polyimide thin film but decreased at the maximum Ni loading of 10 wt%. The trend of $T_{max\ (°C)}$ increased gradually from 529 for pure PI through 535 °C for P-2 and decreased to 528 °C for P-4 as observed in **Table 2**.

The pure polyimide had an average $T_{end}$ of 662 °C and increased to 667 °C for the PI-Ni 10 wt% nanocomposites. The trend in $\Delta T$ °C shows an increase from P-1 pure polyimide to polyimide nanocomposites, increasing from 248 °C to 280 °C for the polyimide with maximum nickel content of 10 wt% under experimental conditions. The increase in $\Delta T$ °C can be attributed to the high heat resistance offered by Ni constituents due to their inorganic nature [32]. However, with increasing Ni filler, the average char residue decreased sharply from 46 to 39 for both 1 wt% and 5 wt% but increased for 10 wt% Ni film. The integration of nanofillers into polymer nanocomposite membranes has been reported to enhance their properties and overall performance in processability [33].



***Non-Isothermal Kinetic Degradation of BPADA-BAPP Polyimide-NiNCs***

The thermal stability of polyimide and polyimide-nickel composite films in relation to nanofiller loading was investigated and discussed at various heating rates. The thermal degradation of polyimides is described by **Equation 2**:

$$A_{solid} \rightarrow B_{solid} + C_{gas} \qquad \textbf{Equation 2}$$

Where A, B and C are the initial polyimide, polymer residue and gas evolved respectively. In such a heterogeneous system the conversion factor (α) indicates the progress of the reaction. The conversion factor (α) is calculated using **Equation 3**.

$$\alpha = \frac{Wo-Wt}{Wo-Wf}$$ **Equation 3**

Where Wo, Wt and Wf represent initial weight at the onset of degradation, actual weight at time t and final weight after degradation respectively. The kinetic models assume the rate of isothermal conversion dα/dt to be linear function of both temperature independent function of the conversion (α) and temperature-dependent rate constant k (T) hence, we can write

$$\frac{d\alpha}{dt} = k(T)f(\alpha)$$ **Equation 4**

Where f (α) is dependent on the mechanism of the decomposition reaction. The Arrhenius equation describes the function k (T) as in **Equation 5**.

$$k(T) = A\, e^{\frac{-E_a}{RT}}$$ **Equation 5**



Where Ea is the activation energy (kJ $mol^{-1}$), A is the pre-exponential factor ($min^{-1}$), R the universal gas constant (8.314 $Jmol^{-1}K^{-1}$) and T the thermodynamic temperature (K). Combining **Equation 4** and **Equation 5** gives

$$\frac{d\alpha}{dt} = A\, f(\alpha) e^{\frac{-E_a}{RT}}$$ **Equation 6**

But $\beta = \frac{dT}{dt}$ at constant heating rate and by substituting the heating rate into **Equation 6** we obtain

$$\beta \frac{d\alpha}{dt} = A\, f(\alpha) e^{\frac{-E_a}{RT}}$$ **Equation 7**

**Equation 7** can be rearranged to give

$$\frac{d\alpha}{dt} = \frac{A}{\beta}\, f(\alpha) e^{\frac{-E_a}{RT}}$$ **Equation 8**

**Equation 8** is the fundamental relation for the evaluation of kinetic parameters using TGA data in accordance with non-isothermal kinetic theory. Integrating **Equation 8** within the limits $(T_0)$ initial temperature and its corresponding degree of conversion $(\alpha_0)$ and peak temperature $(T_P)$ leading to a degree of conversion $(\alpha_p)$ gives **equation 9**,

$$\int_{\alpha_0}^{\alpha_p} \frac{d\alpha}{f(\alpha)} = \frac{A}{\beta} \int_{T_0}^{T_p} e^{\frac{-E_a}{RT}} \qquad \textbf{Equation 9}$$

If $(T_0)$ is low and hence, $\alpha = 0$ and no reaction takes place before the initial temperature $(T_0)$ The integral function of conversion $g(\alpha)$ is obtained by the relation

$$g(\alpha) = \int_{\alpha_0}^{\alpha_p} \frac{d\alpha}{f(\alpha)} = \frac{A}{\beta} \int_{T_0}^{T_0} e^{\frac{-E_a}{RT}}\, dt \qquad \textbf{Equation 10}$$

The activation energy $E_a$ of degradation which is the minimum energy required to start the decomposition process is a bulk parameter in determining the onset thermal decmposition profile of a given material [34]. The $E_a$ can be calculated by substituting into **Equation 10** the values of α degree of weight conversion and β the heating rate.

Considerable dynamic models are available for the estimation of $E_a$ of a kinetic process [35]. However, the most widely used approaches are Kissinger-Akahira-Sunose (K-A-S), Flynn-Wall-Ozawa (F-W-O), and Friedman methods [36]. In F-W-O, K-A-S, and Friedman models, the activation energy can be determined without any assumption regarding $f(\alpha)$ , as such these models are said to be "model free". The $E_a$ magnitude determined from K-A-S and F-W-O models represent a statistical average in the range 0-α. Since $E_a$ can vary with the degree of conversion. K-A-S and F-W-O models gained significance because the results show good consistency between $E_a$ magnitudes obtained by these techniques. In this work, two models were employed for the evaluation of $E_a$ these are Flynn-Wall-Ozawa [37] and Kissinger-Akahira-Sunose [38] methods.

### *Flynn Wall Ozawa (F-W-O) METHOD*

Flynn-Wall-Ozawa model is an integral isoconversional technique for determining the activation energy based on **Equation. 11**.

$$log\beta = log\frac{AE_a}{Rg(\alpha)} - 2.315 - \frac{0.457E_a}{RT}$$ **Equation 11**

Where $E_a$, A, R, α, β, and T represent their conventional notation. At constant value of α, a plot of log β versus 1000/T at various heating rates gives a straight line and the slope of this line is used to determine the value of $E_a$. This technique allows the evaluation of the activation energy without the necessary knowledge of reaction order at the various stages of conversion.

The activation energy $E_a$ (kJmol$^{-1}$) is a significant parameter for the performance analysis of polyimides. In the evaluation of thermal stabilities of polyimides, the greater the value of $E_a$ the more the stability of the polyimide and consequently, the wider the fields of applications. The $E_a$ for PI and PI nanocomposites were obtained by TGA curves at various heating rates from 5, 10, 15, 20, to 25 °C min$^{-1}$. In the F-W-O method series of lines were obtained by the linear fitting of lnβ versus 1000/T at conversions of 0.05, 0.1, 0.2, 0.3, 0.4, 0,5, 0.6, 0.7, 0.8, and 0.9 as presented in **Figure 10**. The $E_a$ values were determined from the slopes of the lines using **Equation 11**.

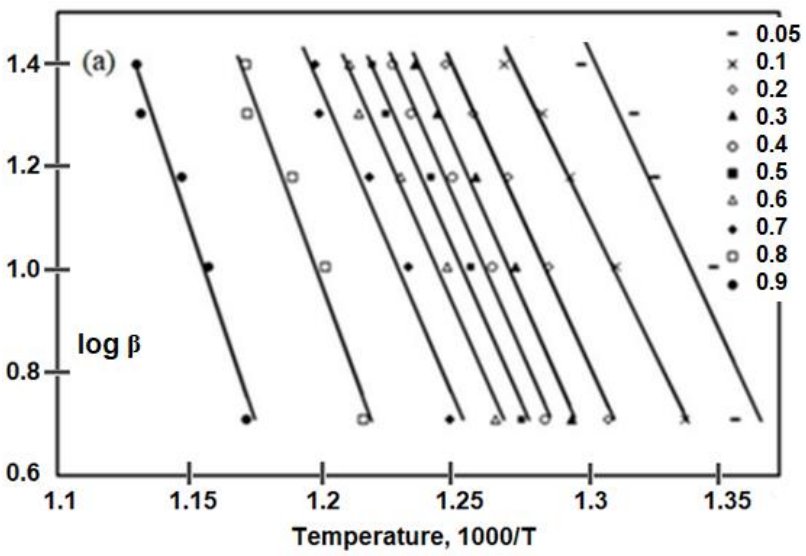

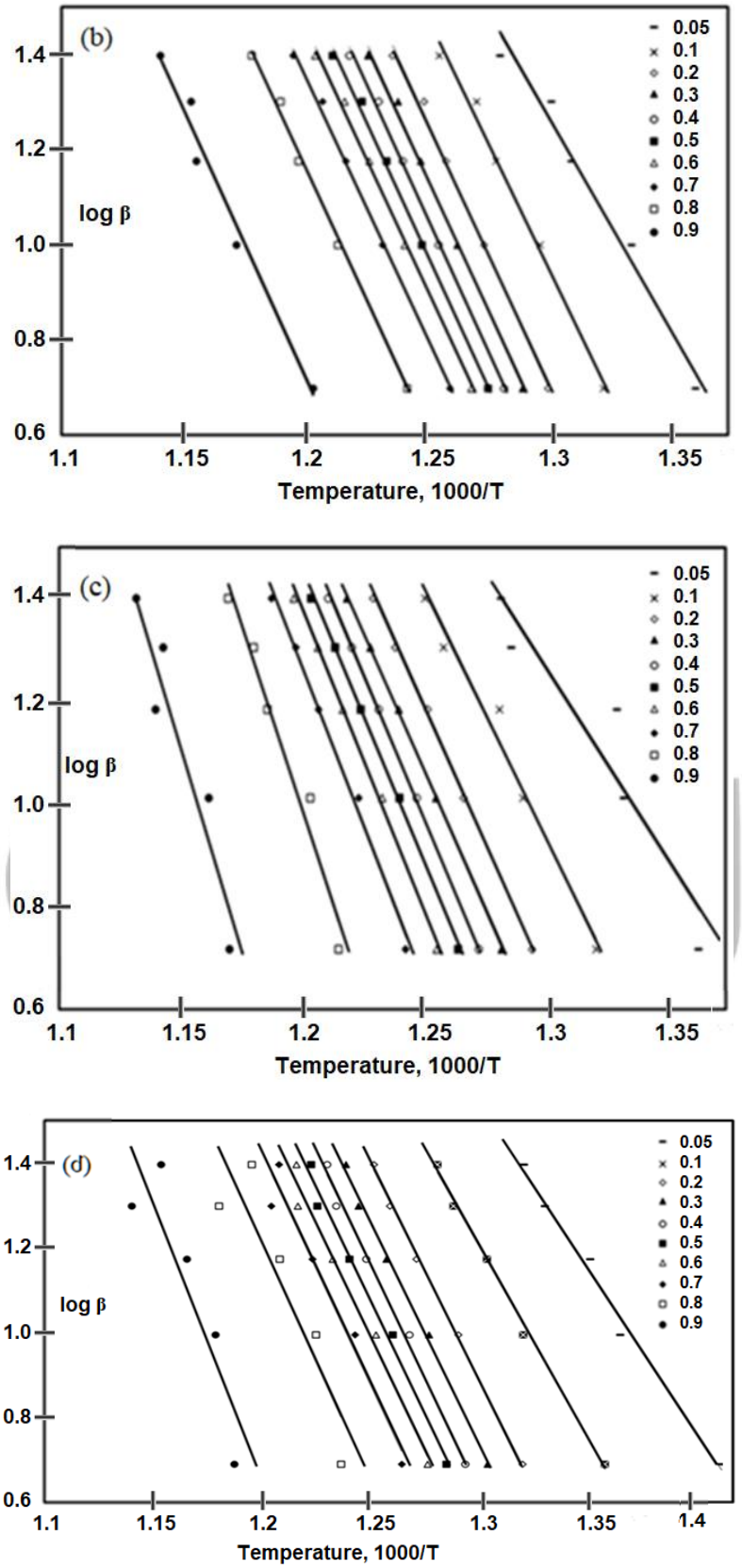


**Figure 10**: F-W-O plots of (a) PI, (b) PI-Ni 1 wt%, (c) PI-Ni 5 wt%, and (d) PI-Ni 10 wt%. Repeated 3 times in each case.

The $E_a$ values (kJmol$^{-1}$) and their corresponding conversions for pure polyimide and polyimide nanocomposites are presented in **Table 3**. The average correlation for PI is 0.9715 and 0.9928, 0.9737 and 0.97528 for PI-Ni 1 wt%, PI-Ni 5 wt%, and PI-Ni 10 wt% respectively. The overall average correlation is 0.9727. At degree of conversion (α = 0.9), it is observed in **Table 3**, that there is a significant increase in the values of $E_a$ from 282.89, 207.52, 301.28, and 237.23 kJmol$^{-1}$ respectively for pure polyimide, PI-Ni 1 wt%, PI-Ni 5 wt%, and PI-Ni 10 wt%. The $E_a$ is observed to increase with increase in weight conversion, indicating a complex reaction in which several mechanisms occur during decomposition [31].

The $E_a$ value increased with increasing Ni filler content [39]. The increasing tendency of $Ea$ coincides with thermal analysis results shown in **Table 3**, suggesting that the polyimide nanocomposites exhibit higher thermal stability. In comparison to pure polyimide, the increase in Ni filler content requires more activation energy for the dissociation of chemical bonds leading to higher values of activation energy [40].

**Table 3** Values of $E_a$ (kJ/mol) and their correlations by F-W-O method. No repetition.

| **Pure PI** | | | **PI-Ni 1 wt%** | | |
|---|---|---|---|---|---|
| **α** | **$E_a$** | **$R^2$** | **α** | **$E_a$** | **$R^2$** |
| 0.05 | 156.08 | 0.8987 | 0.05 | 162.27 | 0.9789 |
| 0.1 | 190.23 | 0.9934 | 0.1 | 194.86 | 0.9922 |
| 0.2 | 207.54 | 0.9932 | 0.2 | 205.83 | 0.9963 |
| 0.3 | 211.90 | 0.9909 | 0.3 | 206.70 | 0.9971 |
| 0.4 | 213.99 | 0.9867 | 0.4 | 206.43 | 0.9973 |
| 0.5 | 214.05 | 0.9818 | 0.5 | 205.23 | 0.9975 |
| 0.6 | 214.94 | 0.9804 | 0.6 | 204.21 | 0.9974 |
| 0.7 | 225.20 | 0.9617 | 0.7 | 203.28 | 0.9976 |
| 0.8 | 256.31 | 0.9609 | 0.8 | 203.95 | 0.996 |
| 0.9 | 282.89 | 0.9673 | 0.9 | 207.52 | 0.9777 |

| **PI-Ni 5 wt%** | **PI-Ni 10 wt%** |
|---|---|

| α | $E_a$ | $R^2$ | α | $E_a$ | $R^2$ |
|---|---|---|---|---|---|
| 0.05 | 140.36 | 0.8985 | 0.05 | 139.92 | 0.9895 |
| 0.1 | 178.96 | 0.9793 | 0.1 | 163.14 | 0.9963 |
| 0.2 | 197.26 | 0.9991 | 0.2 | 182.99 | 0.9987 |
| 0.3 | 203.19 | 0.9997 | 0.3 | 188.63 | 0.9965 |
| 0.4 | 208.45 | 0.9994 | 0.4 | 190.49 | 0.9931 |
| 0.5 | 213.92 | 0.9986 | 0.5 | 192.31 | 0.9893 |
| 0.6 | 219.14 | 0.9971 | 0.6 | 193.98 | 0.9829 |
| 0.7 | 231.75 | 0.9931 | 0.7 | 196.09 | 0.9617 |
| 0.8 | 274.38 | 0.967 | 0.8 | 203.55 | 0.8248 |
| 0.9 | 301.28 | 0.9055 | 0.9 | 237.23 | 0.7959 |

As observed in **Figure 11**, the slope of the curves shows the activation energies, $E_a$ gradually increased with a smooth slope for the Pure PI and PI-NiNCs with different loadings of NiNPs. This increase in $E_a$ with increase in mass conversion indicates the occurrence of a complex reaction involving several steps during thermal degradation. Three steps of $E_a$ have been determined where the first step occur at $\alpha < 0.1$, the second step occur at $0.1 < \alpha < 0.7$ and third step occur at $\alpha < 0.7$. The comparison of the $E_a$ value of pure PI and PI-NiNCs different loading of NiNPs are shown in **Figure 11**.

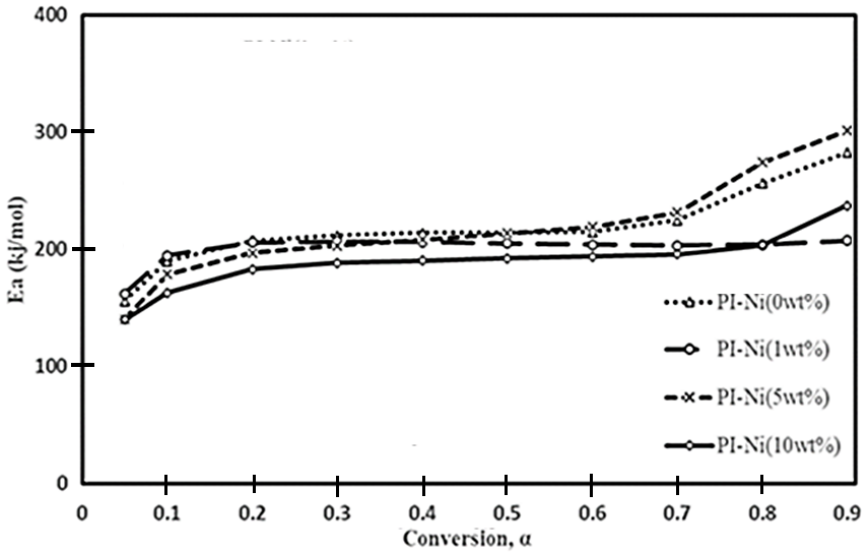

**Figure 11** Plot of $E_a$ against $\alpha$ by F-W-O method for pure PI and PI-Ni composite series.

No repetition.

In the first stage of degradation, the $E_a$ was observed to increase all through the degradation process while in the second decomposition stage, Ea slightly increased all through the decomposition process. The first thermal decomposition process corresponds to the vaporization of air bubbles and water molecules, the second stage is due to dehydration, main chain scission and breaking down of the bond links [41]. However, at the third stage the activation energy suddenly increased. This could be associated with the formation of residue during the thermal decomposition process. The sudden increase in activation energy in PI-NiNCs composite films occurred much faster. This might be associated with the presences of NiNPs dispersed homogenously in the polyimide thin films. The presence of NiNPs in polyimide nanocomposites might hinder the evaporation of volatile component products from the polyimide matrix. The higher the amount of NiNPs in the polyimide matrix, the higher the slope of the $E_a$ curves that will be obtained [42].



***Kissinger-Akahira-Sunose (K-A-S) Model***

The K-A-S model is the most superior when compared to other kinetic models since prior knowledge of reaction order is not required for calculating the values of activation energy [43]. The K-A-S model is an isoconversional approach for the evaluation of the $E_a$ in reactions involving solid-state. Based on **Equation 6** at a constant heating rate $\beta = \frac{dT}{dt}$ therefore.

$$\beta \frac{d\alpha}{dT} = A\, f(\alpha)\, e^{\frac{-E_a}{RT}} \qquad \textbf{Equation 12}$$

$$ln\frac{\beta}{T^2} = \ln\frac{AR}{Eg(\alpha)} - \frac{-E_a}{RT} \qquad \textbf{Equation 13}$$

Where $g(\alpha)$ is the algebraic integral expression. The $E_a$ is evaluated by employing **Equation 13**. The plot of $\frac{\beta}{T^2}$) versus $\frac{1}{T}$ obtained at various heating rates yields a straight line having a gradient equal to $E_a$ of the thermal degradation reaction.

The linear fitting of $\ln\frac{\beta}{T^2}$ versus $\frac{1000}{T}$ gave lines as presented in **Figure 12**. The activation energy values for various conversions of PI and PI nanocomposites are presented in **Table 4**. The average correlation for PI, PI-Ni 1 wt%, PI-Ni 5 wt% and PI-Ni 10 wt% are 0.9713, 0.9920, 0.9702, and 0.9475 respectively and overall average correlation of 0.9702.

In the K-A-S method, straight lines were obtained throughout the conversions from 0.05 to 0.9. In K-A-S model activation energy is derived using peak temperature involving maximum reaction rate. This model is represented with relatively high average correlation of 0.9702, ranging from 0.7758 to 0.9996 of the experimental data in **Table 4**, reliably indicating that this method can be employed to illustrate the thermal properties of polyimide and polyimide-nickel nanocomposites. Like F-W-O method, the kinetic characteristics are altered with the heating rates applied to Ni nanoparticles in the polyimide matrix.

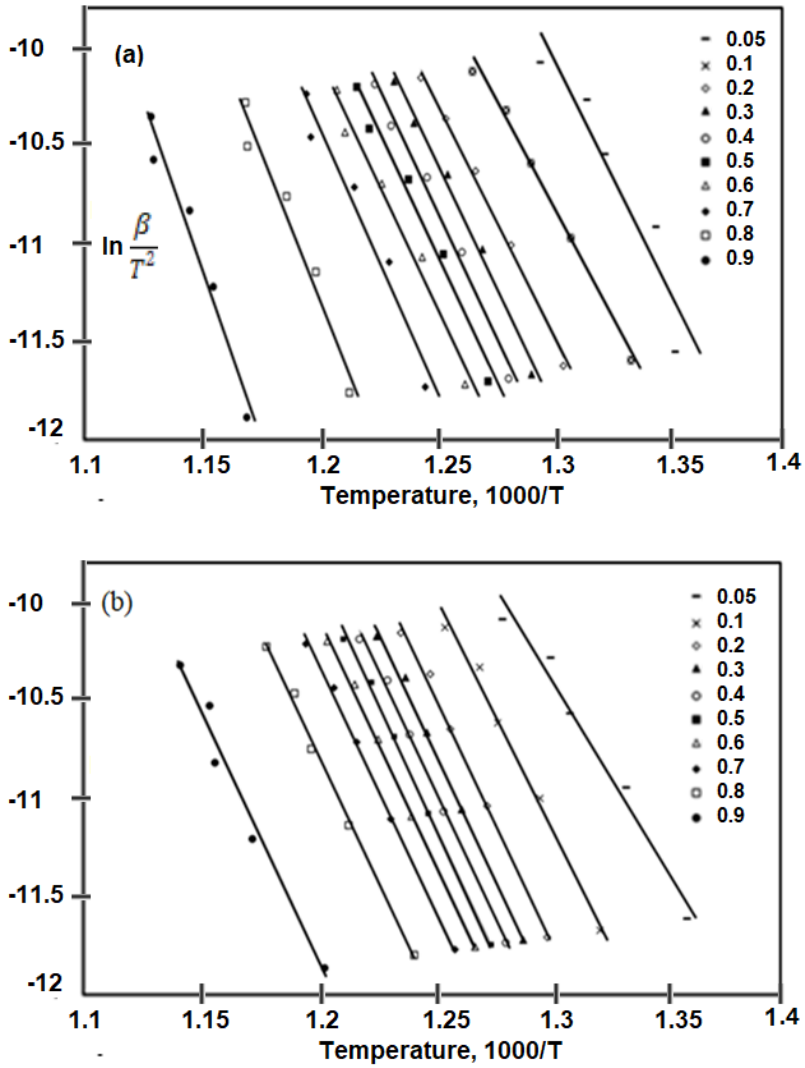

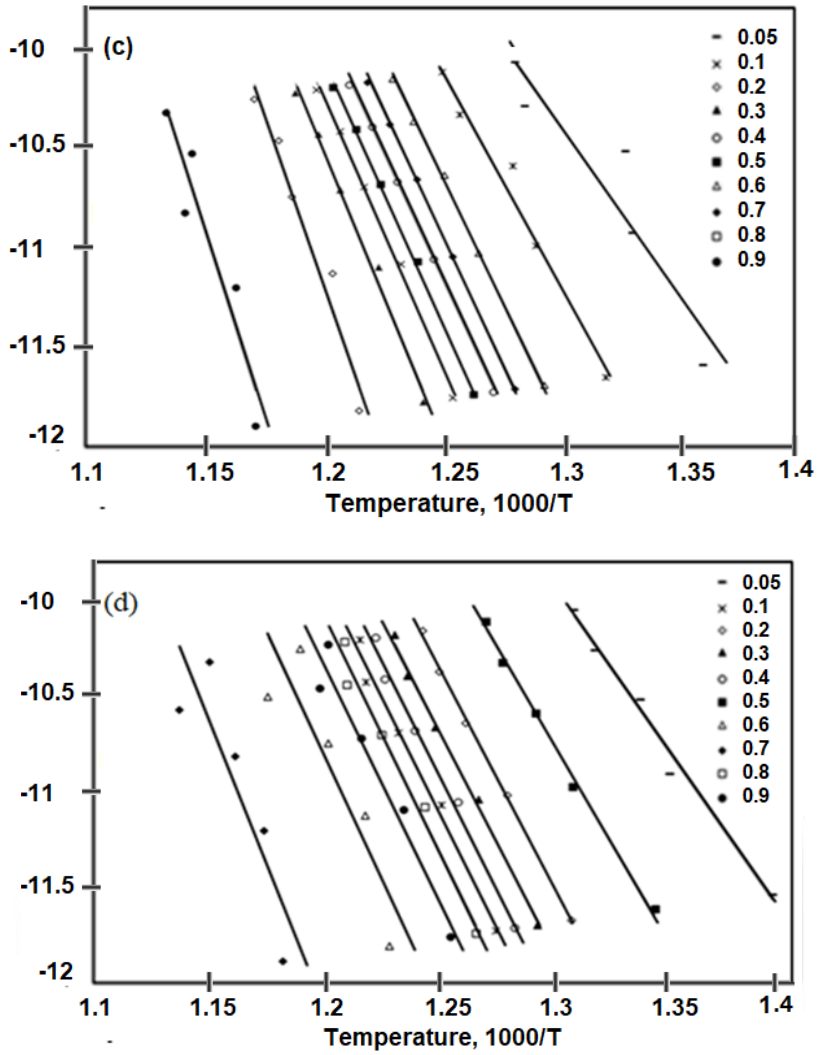


**Figure 12** K-A-S plots of (a) pure PI (b) PI-Ni 1 wt%, (c) PI-Ni 5 wt%, and (d) PI-Ni 10 wt%.

Repeated 3 times.

**Table 4** The values of $E_a$ (kJ/mol) and their correlations by K-A-S method. No repetition.

| PI | | | PI-Ni (1 wt%) | | |
|---|---|---|---|---|---|
| α | $E_a$ | $R^2$ | α | $E_a$ | $R^2$ |
| 0.05 | 197.94 | 0.8965 | 0.05 | 158.14 | 0.9753 |
| 0.1 | 184.18 | 0.9985 | 0.1 | 192.13 | 0.9911 |
| 0.2 | 199.91 | 0.9949 | 0.2 | 203.47 | 0.9957 |
| 0.3 | 207.20 | 0.9911 | 0.3 | 204.27 | 0.9967 |
| 0.4 | 209.97 | 0.9862 | 0.4 | 203.99 | 0.997 |
| 0.5 | 210.17 | 0.9806 | 0.5 | 203.61 | 0.9978 |
| 0.6 | 210.78 | 0.9791 | 0.6 | 202.52 | 0.9977 |
| 0.7 | 219.87 | 0.9601 | 0.7 | 201.72 | 0.998 |
| 0.8 | 247.98 | 0.9619 | 0.8 | 203.42 | 0.996 |
| 0.9 | 283.19 | 0.964 | 0.9 | 204.19 | 0.9746 |

| PI-Ni(5 wt%) | | | PI-Ni(10 wt%) | | |
|---|---|---|---|---|---|
| α | $E_a$ | $R^2$ | α | $E_a$ | $R^2$ |
| 0.05 | 135.11 | 0.8808 | 0.05 | 135.06 | 0.9877 |
| 0.1 | 175.39 | 0.9761 | 0.1 | 159.06 | 0.9957 |
| 0.2 | 194.43 | 0.999 | 0.2 | 179.64 | 0.9985 |
| 0.3 | 200.55 | 0.9996 | 0.3 | 185.42 | 0.9960 |
| 0.4 | 205.97 | 0.9993 | 0.4 | 187.27 | 0.9921 |
| 0.5 | 211.65 | 0.9984 | 0.5 | 189.08 | 0.9878 |
| 0.6 | 217.05 | 0.9966 | 0.6 | 190.77 | 0.9804 |
| 0.7 | 230.16 | 0.9922 | 0.7 | 192.86 | 0.9563 |
| 0.8 | 274.55 | 0.9633 | 0.8 | 200.44 | 0.8045 |
| 0.9 | 301.96 | 0.8968 | 0.9 | 235.34 | 0.7758 |

The $E_a$ and $R^2$ values exhibit similar trend in behavior to the average values calculated using F-W-O model. Notwithstanding, there are differences in numerical values of the kinetic parameters in the F-W-O and K-A-S models. The differences with respect to F-W-O and K-A-S models arise from the mathematical equations of the two methods represented by **Equation 11** for F-W-O and **Equation 13** for K-A-S models. The average correlation value obtained by F-W-O is 0.9727 and 0.9702 for K-A-S model are close suggesting the reliability of both methods. The results obtained in this work are consistent with those reported Yousef et al [43]. The plots of $E_a$ against α by K-A-S method for pure PI and PI-NiNCs series are shown in **Figure 13**.

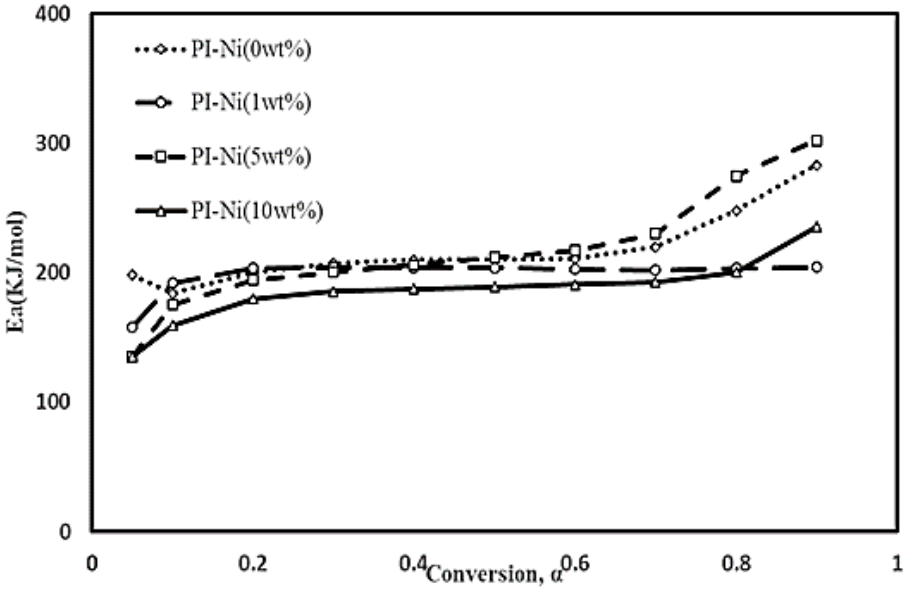


**Figure 13** Plot of $E_a$ against $\alpha$ by K-A-S method for pure PI and PI-NiNCs series.

Repeated 3 times.

As seen in **Figure 13**, the activation energies are represented by the slope of the curves, similarly observed in **Figure 11**. The slope of the curves shows $E_a$ increasing gradually with smooth slope for PI and PI-NiNCs with different loadings of NiNPs. The increase in $E_a$ with increasing mass conversion indicates the presence of a complex reaction involving several step processes occurring during degradation. Three steps of $E_a$ have been determined where the first step occur at α < 0.1, the second step occur at 0.1 < α < 0.7 and third step occur at α < 0.7. As observed in **Figure 11**, the slope of the curves shows the $E_a$ increasing gradually with smooth gradient for PI and PI-NiNCs with different loadings of NiNPs.

In the first decomposition stage, the activation energy obviously increased all through the decomposition process except for the $E_a$ of Pure PI as shown in **Figure 13**. In the second decomposition stage, the activation energy increased gradually throughout the decomposition process. This decomposition process is attributed to the breaking down of the weak links [44]. However, at the third stage a sudden increase in activation energy is observed. The sudden increase in $E_a$ of PI-Ni composite films occurred at a fast rate. The higher the amount of NiNPs in the polyimide matrix, the higher the slope of the $E_a$ curve obtained [45].

In the polyimide and composite series, presented in **Figure 13**, the value of $E_a$ decreased in the following order, PI-Ni 5 wt% > Pure PI > PI-Ni 10 wt% > PI-Ni 1 wt%. As presented in **Figure 13**, the slope of curve for PI-Ni 1 wt% shows flat curve of activation energy as conversion increased from 0.05 to 0.9. From the $E_a$ listed in **Table 4**, the $E_a$ for PI-Ni 1 wt% shows slight increasing of $E_a$ as the conversion increased. This might be due to the presence of too little amount of NiNPs are not enough to homogenously dispersed in the polyimide matrix. As compared to slope of $E_a$ curves for Pure PI with the PI-Ni 1 wt%, the PI exhibit better thermal stability compared to PI-Ni 1 wt%.

When the NiNPs loading is increased, the slope of the curves shows the $E_a$ gradually increased as the conversion increases. This is clearly observed when we compared the slope of the $E_a$ curve for Pure PI with the PI-Ni 5 wt% from the **Figure 13**. However, when the NiNPs is increased to 10 wt%, the slope of $E_a$ curve shows a decreasing trend compared to PI-Ni 5 wt% and Pure PI. This indicates that PI-Ni 10 wt% is less stable compared to PI-Ni 5 wt%, PI-Ni 1 wt% and Pure PI. This could be due to the lack of even dispersion of NiNPs in the polyimide thin films leading to lower values of $E_a$ in PI-Ni 10 wt%.

### *Activation Energy of BAPP-BPADA Polyimide-NiNCs*

In the PI-Ni nanocomposites, as carbon tends to diffuse along grain boundaries, organic residue segregates to the grain boundaries of the Ni metal leading to contamination. The grain boundary has been suggested to cause intergranular fracture [46]. Further comparison average activation energies correlations at various conversions from 5% to 90%, for F-W-O and K-A-S models are shown in **Table 5**. The average correlations for F-W-O and K-A-S models are greater than 0.97 suggesting a relatively good fit. The trend for K-A-S shows a steady rise in $E_a$ with increasing Ni loading from 1 wt% to 10 wt% Ni.

The derived $E_a$ in both models reveal a good correlation with Ni filler content, increasing with increase in Ni nanoparticles in the polyimide matrix. The high activation energy of the polyimide nanocomposites compared to the

pure polyimide indicate the nanocomposites dissipates more energy and is more heat resistant. Under high heating rate, the polyimide chains could be frozen suddenly after heat treatment, and luck the time to conform or move to form perfect lattice leading to greater residual stress evidently affecting the kinetic characteristics [47]. The results for K-A-S and F-W-O models revealed that at 0.9 conversions, the fittings are not very good, suggesting complex reaction mechanism at this stage.

**Table 5** Average activation energies and average correlations for F-W-O and K-A-S methods. No repetition.

| **F-W-O** | | | **K-A-S** | | | $\Delta E_a$ |
|---|---|---|---|---|---|---|
| **α** | $E_a$ **(kJ/mol)** | $R^2$ | **α** | $E_a$ **(kJ/mol)** | $R^2$ | $E_{a\ \text{F-W-O}} - E_{a\ \text{K-A-S}}$ |
| **Pure PI** | | | | | | |
| 0.05 | 156.0885 | 0.8987 | 0.05 | 197.9480 | 0.8965 | -41.8595 |
| 0.1 | 190.2396 | 0.9934 | 0.1 | 184.1800 | 0.9985 | 6.0596 |
| 0.2 | 207.5407 | 0.9932 | 0.2 | 199.9184 | 0.9949 | 7.6223 |
| 0.3 | 211.9069 | 0.9909 | 0.3 | 207.2015 | 0.9911 | 4.7054 |
| 0.4 | 213.9991 | 0.9867 | 0.4 | 209.9784 | 0.9862 | 4.0207 |
| 0.5 | 214.0537 | 0.9818 | 0.5 | 210.1779 | 0.9806 | 3.8758 |
| 0.6 | 214.9451 | 0.9804 | 0.6 | 210.7848 | 0.9791 | 4.1603 |
| 0.7 | 225.2057 | 0.9617 | 0.7 | 219.8720 | 0.9601 | 5.3337 |
| 0.8 | 256.3150 | 0.9609 | 0.8 | 247.9817 | 0.9619 | 8.3333 |
| 0.9 | 282.8943 | 0.9673 | 0.9 | 283.1998 | 0.9640 | -0.3055 |
| **PI-Ni 1wt%** | | | | | | |
| 0.05 | 162.2776 | 0.9789 | 0.05 | 158.1489 | 0.9753 | 4.1287 |
| 0.1 | 194.8605 | 0.9922 | 0.1 | 192.1365 | 0.9911 | -3.276 |
| 0.2 | 205.8306 | 0.9963 | 0.2 | 203.4768 | 0.9957 | 2.3538 |
| 0.3 | 206.7039 | 0.9971 | 0.3 | 204.2750 | 0.9967 | 2.4289 |
| 0.4 | 206.4310 | 0.9973 | 0.4 | 203.9923 | 0.997 | 2.4387 |
| 0.5 | 205.2303 | 0.9975 | 0.5 | 203.6182 | 0.9978 | 1.6121 |
| 0.6 | 204.2115 | 0.9974 | 0.6 | 202.5207 | 0.9977 | 1.6908 |

| | | | | | | |
|---|---|---|---|---|---|---|
| 0.7 | 203.2837 | 0.9976 | 0.7 | 201.7226 | 0.998 | 1.5611 |
| 0.8 | 203.9568 | 0.996 | 0.8 | 203.4270 | 0.996 | 0.5298 |
| 0.9 | 207.5225 | 0.9777 | 0.9 | 204.1918 | 0.9746 | 3.3307 |
| **PI-Ni 5wt%** | | | | | | |
| 0.05 | 140.3683 | 0.8985 | 0.05 | 135.1108 | 0.8808 | 5.2575 |
| 0.1 | 178.9639 | 0.9793 | 0.1 | 175.3921 | 0.9761 | 3.5718 |
| 0.2 | 197.2619 | 0.9991 | 0.2 | 194.4312 | 0.999 | 2.8307 |
| 0.3 | 203.1927 | 0.9997 | 0.3 | 200.5503 | 0.9996 | 2.6424 |
| 0.4 | 208.4504 | 0.9994 | 0.4 | 205.9710 | 0.9993 | 2.4794 |
| 0.5 | 213.9263 | 0.9986 | 0.5 | 211.6578 | 0.9984 | 2.2685 |
| 0.6 | 219.1476 | 0.9971 | 0.6 | 217.0536 | 0.9966 | 2.094 |
| 0.7 | 231.7550 | 0.9931 | 0.7 | 230.1648 | 0.9922 | 1.5902 |
| 0.8 | 274.3802 | 0.967 | 0.8 | 274.5532 | 0.9633 | -0.173 |
| 0.9 | 301.2870 | 0.9055 | 0.9 | 301.9645 | 0.8968 | -0.6775 |
| **PI-Ni 10wt%** | | | | | | |
| 0.05 | 139.9208 | 0.9895 | 0.05 | 135.0692 | 0.9877 | 4.8516 |
| 0.1 | 163.1400 | 0.9963 | 0.1 | 159.0634 | 0.9957 | 4.0766 |
| 0.2 | 182.9990 | 0.9987 | 0.2 | 179.6406 | 0.9985 | 3.3584 |
| 0.3 | 188.6387 | 0.9965 | 0.3 | 185.4271 | 0.996 | 3.2116 |
| 0.4 | 190.4943 | 0.9931 | 0.4 | 187.2729 | 0.9921 | 3.2214 |
| 0.5 | 192.3136 | 0.9893 | 0.5 | 189.0853 | 0.9878 | 3.2283 |
| 0.6 | 193.9873 | 0.9829 | 0.6 | 190.7730 | 0.9804 | 3.2143 |
| 0.7 | 196.0976 | 0.9617 | 0.7 | 192.8682 | 0.9563 | 3.2294 |
| 0.8 | 203.5566 | 0.8248 | 0.8 | 200.4422 | 0.8045 | 3.1144 |
| 0.9 | 237.2310 | 0.7959 | 0.9 | 235.3444 | 0.7758 | 1.8866 |

The evidence contained in **Table 5** show that in the F-W-O method the addition of Ni lowered the activation energy required to initiate the thermal decomposition of the polyimide nanocomposites. At maximum conversion

in the K-A-S method, the results show significant decrease in average $E_a$ values from 217, 197, 214 and 185 kJmol$^{-1}$ for PI, PI-Ni 1 wt%, PI-Ni 5 wt%, and PI-Ni 10 wt% respectively. Comparison of the average $E_a$ by F-W-O and K-A-S models shows close result with higher K-A-S values than F-W-O model as in **Figure 14**.

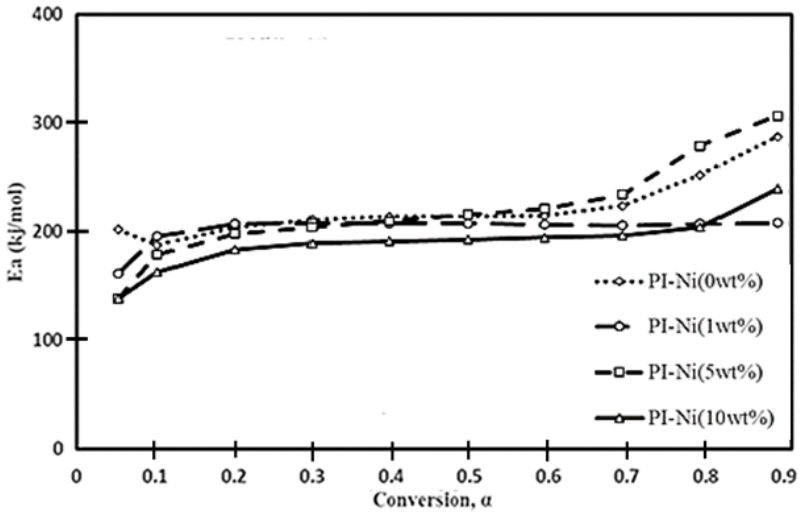


**Figure 14:** (a) Plot of Ea against α by F-W-O and (b) Plot of Ea against α by K-A-S.

Repeated 3 times.



The plots show similar trends confirming the reliability of F-W-O and K-A-S models in the determination of Ea from thermogravimetric analysis of polyimides. From the obtained activation energies, it can be observed that The faster the heating rate, the less chance of solid-state sintering occurring before surface melting occurs. Therefore, at faster heating rate less $E_a$ is required as compared to slower heating rate [42]. Higher heating rates will lead to crystallinity and improve tensile moduli in polyimide fibers. At the beginning decomposition, the release of volatile components occurs in a major proportion, thereafter the reactions at α values of 0.7, 0.8, and 0.9 reveal decomposition resulting from chain scissions of polyimide particles that were spurred due to the presence of NiNPs in the polyimide matrix.

## Conclusions

A series of polyimide-nickel composites were successfully fabricated by a two-step solution blending approach. The structural characteristics of pure polyimide were determined using FT-IR and H-NMR spectroscopy. The structure of pure polyimide was confirmed with H-NMR. Whereas FT-IR was used to determine the presence of

imide group in the polyimide. FT-IR absorbance spectra was employed to evaluate the degree of imidization of the PI series. Free volume expectedly increased owing to the disturbance of the dense packing in polyimide backbone chain. The distribution of Ni nanoparticles in the polyimide thin films was verified the presence of Ni in the EDX, whose signal increased with increasing Ni filler loads. SEM images showed Ni incorporated in the polyimide matrix, proving that the polyimide bonded well with Ni. The TGA results reveal a double-stage decomposition process for the polyimide series. The maximum degradation temperature and char yield increased with increasing Ni filler content. The prepared polyimide series were found to be soluble in polar protic solvents, hence, their ease of processability. However, to significantly enhance the mechanical, electrical, and thermal properties of the polyimide, higher loads of Ni filler are required. Ni nanoparticles exhibit excellent compatibility as well as adhesion in the polyimide matrix. However, it is observed that certain sites of Ni nanoparticles in the PI matrix tend to form large agglomerates with increasing Ni content. Ni nanoparticles were successfully incorporated into BPADA-BAPP polyimide solution blending at I wt%, 5 wt%, and 10 wt% loading, thereby reducing the chain mobility of polyimide segments. The TGA analysis were performed at rates of 5, 10, 15, 20, and 25°C/min to evaluate the degradation kinetics. F-W-O and K-A-S models were employed for the evaluation of $E_a$. The $E_a$ of pure polyimide and polyimide nanocomposites were calculated at various heating rates and degrees of conversion using the two models. The results obtained for both models indicated an increase in stability with increase in filler loading. The results generated by F-W-O and K-A-S models showed good agreement for the fitting and $E_a$ values. The lifetime of the fabricated polyimide nanocomposites can be generated from the TGA apparent kinetic parameters. Lifetime estimates are critical in the design, selection, and development of polymers for specific industrial applications. Additionally, the polyimide-nicked nanocomposites can be used in electrical and electrochemical applications as conductive films.

## Acknowledgments

The authors would like to thank the School of Chemical Sciences, Universiti Sains Malaysia for technical support.

## Funding Information

The authors wish to acknowledge Universiti Sains Malaysia for FRGS/1/2020/STG05/USM/02/3 awarded by the Ministry of Higher Education Malaysia. Nuru-Deen Jaji wishes to thank the Federal College of Education Technical Gombe, Nigeria, for TETFUND PhD Scholarship.

## Author Contributions

Muhammad Bisyrul Hafi Othman: conceptualization and resources. Nuru-Deen Jaji: formal analysis and investigation. Muhammad Bisyrul Hafi: Nuru-Deen Jaji, Yong Shen Chua, Hammam Abdurabu Thabit: data curation, writing, and original draft preparation. Muhammad Bisyrul Hafi Othman: project administration. All authors have accepted responsibility for the entire content of this manuscript and approved its submission.

## Conflict Of Interest

The authors declare that they have no conflict of interest.



## References

[1] V. S. Chandel, G. Wang, and M. Talha, "Advances in modelling and analysis of nano structures: a review," *Nanotechnol. Rev.*, vol. 9, no. 1, pp. 230–258, Mar. 2020, doi: 10.1515/ntrev-2020-0020.
[2] N.-D. Jaji, H. L. Lee, M. H. Hussin, H. M. Akil, M. R. Zakaria, and M. B. H. Othman, "Advanced nickel nanoparticles technology: From synthesis to applications," *Nanotechnol. Rev.*, vol. 9, no. 1, pp. 1456–1480, Dec. 2020, doi: 10.1515/ntrev-2020-0109.
[3] M. Malaki and R. S. Varma, "Mechanotribological Aspects of MXene-Reinforced Nanocomposites," *Adv. Mater.*, vol. 32, no. 38, p. 2003154, Sep. 2020, doi: 10.1002/adma.202003154.
[4] N.-D. Jaji *et al.*, "Polyimide–nickel nanocomposites fabrication, properties, and applications: A review," *Rev. Adv. Mater. Sci.*, vol. 62, no. 1, p. 20230113, Sep. 2023, doi: 10.1515/rams-2023-0113.
[5] X. Wang *et al.*, "Comparative Study of Three Carbon Additives: Carbon Nanotubes, Graphene, and Fullerene-C60, for Synthesizing Enhanced Polymer Nanocomposites," *Nanomaterials*, vol. 10, no. 5, p. 838, Apr. 2020, doi: 10.3390/nano10050838.
[6] M. B. H. Othman, Z. Ahmad, H. M. Akil, M. R. Zakaria, and F. Ullah, "The effects of the SiOSi segment presence in BAPP/BPDA polyimide system on morphology and hardness properties for opto-electronic application," *Mater. Des.*, vol. 82, pp. 98–105, Oct. 2015, doi: 10.1016/j.matdes.2015.05.054.
[7] Z. Lan, C. Li, Y. Yu, and J. Wei, "Colorless Semi-Alicyclic Copolyimides with High Thermal Stability and Solubility," *Polymers*, vol. 11, no. 8, p. 1319, Aug. 2019, doi: 10.3390/polym11081319.
[8] D. Coetzee, M. Venkataraman, J. Militky, and M. Petru, "Influence of Nanoparticles on Thermal and Electrical Conductivity of Composites," *Polymers*, vol. 12, no. 4, p. 742, Mar. 2020, doi: 10.3390/polym12040742.
[9] N.-D. Jaji, M. B. H. Othman, H. L. Lee, M. H. Hussin, and D. Hui, "One-pot solvothermal synthesis and characterization of highly stable nickel nanoparticles," *Nanotechnol. Rev.*, vol. 10, no. 1, pp. 318–329, May 2021, doi: 10.1515/ntrev-2021-0019.
[10] Y. She *et al.*, "Block-Co-polymer-Assisted Synthesis of All Inorganic Highly Porous Heterostructures with Highly Accessible Thermally Stable Functional Centers," *ACS Appl. Mater. Interfaces*, vol. 11, no. 33, pp. 30154–30162, Aug. 2019, doi: 10.1021/acsami.9b09991.
[11] S. A. Mamuru and N. Jaji, "Voltammetric and impedimetric behaviour of phytosynthesized nickel nanoparticles," *J. Nanostructure Chem.*, vol. 5, no. 4, pp. 347–356, Dec. 2015, doi: 10.1007/s40097-015-0166-x.
[12] T. Nejatian, N. Nathwani, L. Taylor, and F. Sefat, "Denture Base Composites: Effect of Surface Modified Nano- and Micro-Particulates on Mechanical Properties of Polymethyl Methacrylate," *Materials*, vol. 13, no. 2, p. 307, Jan. 2020, doi: 10.3390/ma13020307.
[13] P. Okafor and J. Iroh, "Electrochemical Properties of Porous Graphene/Polyimide-Nickel Oxide Hybrid Composite Electrode Material," *Energies*, vol. 14, no. 3, p. 582, Jan. 2021, doi: 10.3390/en14030582.

[14] M. Yoonessi *et al.*, "High-temperature multifunctional magnetoactive nickel graphene polyimide nanocomposites," *Polymer*, vol. 54, no. 11, pp. 2776–2784, May 2013, doi: 10.1016/j.polymer.2013.03.015.
[15] W. Gao *et al.*, "Efficient carbon nanotube/polyimide composites exhibiting tunable temperature coefficient of resistance for multi-role thermal films," *Compos. Sci. Technol.*, vol. 199, p. 108333, Oct. 2020, doi: 10.1016/j.compscitech.2020.108333.
[16] M. B. H. Othman, H. M. Akil, H. Osman, A. Khan, and Z. Ahmad, "Synthesis, characterisation and thermal properties of hyperbranched polyimide derived from melamine via emulsion polymerisation," *J. Therm. Anal. Calorim.*, vol. 120, no. 3, pp. 1785–1798, Jun. 2015, doi: 10.1007/s10973-015-4464-9.
[17] D. Lin, Y. Liu, Z. Jia, S. Qi, and D. Wu, "Structural Evolution of Macromolecular Chain During Pre-imidization Process and Its Effects on Polyimide Film Properties," *J. Phys. Chem. B*, vol. 124, no. 36, pp. 7969–7978, Sep. 2020, doi: 10.1021/acs.jpcb.0c05146.
[18] D. Li *et al.*, "Preparation of PI/PTFE–PAI Composite Nanofiber Aerogels with Hierarchical Structure and High-Filtration Efficiency," *Nanomaterials*, vol. 10, no. 9, p. 1806, Sep. 2020, doi: 10.3390/nano10091806.
[19] G. Qiu, W. Ma, and L. Wu, "Thermoplastic and low dielectric constants polyimides based on BPADA-BAPP," *Polym.-Plast. Technol. Mater.*, vol. 59, no. 13, pp. 1482–1491, Sep. 2020, doi: 10.1080/25740881.2020.1750651.
[20] C. A. Terraza, R. Martin-Trasanco, C. Saldías, M. González, Á. Leiva, and A. Tundidor-Camba, "Preparation of CuONPs@PVDF/Non-Woven Polyester Composite Membrane: Structural Influence of Nanoparticle Addition," *Polymers*, vol. 10, no. 8, p. 862, Aug. 2018, doi: 10.3390/polym10080862.
[21] H. Huang, C. Karlsson, M. Strømme, A. Gogoll, and M. Sjödin, "Synthesis and characterization of poly-3-((2,5-hydroquinone)vinyl)-1H-pyrrole: investigation on backbone/pendant interactions in a conducting redox polymer," *Phys. Chem. Chem. Phys.*, vol. 19, no. 16, pp. 10427–10435, 2017, doi: 10.1039/C6CP08736A.
[22] M. Hasegawa, "Development of Solution-Processable, Optically Transparent Polyimides with Ultra-Low Linear Coefficients of Thermal Expansion," *Polymers*, vol. 9, no. 10, p. 520, Oct. 2017, doi: 10.3390/polym9100520.
[23] E. Tarani *et al.*, "Influence of Graphene Platelet Aspect Ratio on the Mechanical Properties of HDPE Nanocomposites: Microscopic Observation and Micromechanical Modeling," *Polymers*, vol. 12, no. 8, p. 1719, Jul. 2020, doi: 10.3390/polym12081719.
[24] R. Castro-Muñoz, M. Z. Ahmad, and V. Fíla, "Tuning of Nano-Based Materials for Embedding Into Low-Permeability Polyimides for a Featured Gas Separation," *Front. Chem.*, vol. 7, p. 897, Jan. 2020, doi: 10.3389/fchem.2019.00897.
[25] M. B. H. Othman, M. R. Ramli, L. Y. Tyng, Z. Ahmad, and H. Md. Akil, "Dielectric constant and refractive index of poly (siloxane–imide) block copolymer," *Mater. Des.*, vol. 32, no. 6, pp. 3173–3182, Jun. 2011, doi: 10.1016/j.matdes.2011.02.048.
[26] N. H. Suhaimi, Y. F. Yeong, C. W. M. Ch'ng, and N. Jusoh, "Tailoring CO2/CH4 Separation Performance of Mixed Matrix Membranes by Using ZIF-8 Particles Functionalized with Different Amine Groups," *Polymers*, vol. 11, no. 12, p. 2042, Dec. 2019, doi: 10.3390/polym11122042.
[27] H. A. Thabit *et al.*, "Investigation of the thermoluminescence dosimeter characteristics of multilayer ZnO(300 nm)/Ag(50 nm)/ZnO(x) thin films for photonic dosimetry applications," *Opt. Mater.*, vol. 137, p. 113548, Mar. 2023, doi: 10.1016/j.optmat.2023.113548.
[28] Z.-C. Ma *et al.*, "Intense Femtosecond Laser-Mediated Electrical Discharge Enables Preparation of Amorphous Nickel Phosphide Nanoparticles," *Langmuir*, vol. 34, no. 20, pp. 5712–5718, May 2018, doi: 10.1021/acs.langmuir.7b04190.
[29] M. Hajibeygi, M. Maleki, and M. Shabanian, "The effects of poly(amide-imide) coating on the thermal, combustion and mechanical properties of polyvinyl chloride ZnO nanocomposites," *Prog. Org. Coat.*, vol. 122, pp. 96–106, Sep. 2018, doi: 10.1016/j.porgcoat.2018.05.013.
[30] F. Zhu, Y. Xu, Q. Feng, and Q. Yang, "Thermal kinetics study and flammability evaluation of polyimide fiber material," *J. Therm. Anal. Calorim.*, vol. 131, no. 3, pp. 2579–2587, Mar. 2018, doi: 10.1007/s10973-017-6752-z.
[31] X. Su, Y. Xu, L. Li, and C. Song, "Characterization and thermal degradation kinetics of thermoplastic polyimide based on BAPP," *High Perform. Polym.*, vol. 30, no. 7, pp. 787–793, Sep. 2018, doi: 10.1177/0954008317729741.
[32] M. Hatami and M. Yazdan Panah, "Ultrasonic assisted synthesis of nanocomposite materials based on resole resin and surface modified nano CeO2: Chemical and morphological aspects," *Ultrason. Sonochem.*, vol. 39, pp. 160–173, Nov. 2017, doi: 10.1016/j.ultsonch.2017.04.028.
[33] T. Van Den Berg and M. Ulbricht, "Polymer Nanocomposite Ultrafiltration Membranes: The Influence of Polymeric Additive, Dispersion Quality and Particle Modification on the Integration of Zinc Oxide Nanoparticles into Polyvinylidene Difluoride Membranes," *Membranes*, vol. 10, no. 9, p. 197, Aug. 2020, doi: 10.3390/membranes10090197.
[34] E. A. Franco-Urquiza, J. F. May-Crespo, C. A. Escalante Velázquez, R. Pérez Mora, and P. González García, "Thermal Degradation Kinetics of ZnO/polyester Nanocomposites," *Polymers*, vol. 12, no. 8, p. 1753, Aug. 2020, doi: 10.3390/polym12081753.
[35] R. Wei, D. Xiang, H. Long, C. (Charles) Xu, and J. Li, "Reduction of iron oxide by lignin: Characteristics, kinetics and superiority," *Energy*, vol. 197, p. 117203, Apr. 2020, doi: 10.1016/j.energy.2020.117203.
[36] A. A. Stolov and D. A. Simoff, "Thermal stability of optical fiber coatings: comparison of experimental thermogravimetric approaches," *J. Therm. Anal. Calorim.*, vol. 146, no. 4, pp. 1773–1789, Nov. 2021, doi: 10.1007/s10973-020-10146-7.
[37] A. Mittal, S. Garg, and S. Bajpai, "Thermal decomposition kinetics and properties of grafted barley husk reinforced PVA/starch composite films for packaging applications," *Carbohydr. Polym.*, vol. 240, p. 116225, Jul. 2020, doi: 10.1016/j.carbpol.2020.116225.
[38] R. K. Singh, D. Pandey, T. Patil, and A. N. Sawarkar, "Pyrolysis of banana leaves biomass: Physico-chemical characterization, thermal decomposition behavior, kinetic and thermodynamic analyses," *Bioresour. Technol.*, vol. 310, p. 123464, Aug. 2020, doi: 10.1016/j.biortech.2020.123464.
[39] L. Nayak, M. Rahaman, D. Khastgir, and T. K. Chaki, "Thermal degradation kinetics of polyimide nanocomposites from different carbon nanofillers: Applicability of different theoretical models," *J. Appl. Polym. Sci.*, vol. 135, no. 7, p. 45862, Feb. 2018, doi: 10.1002/app.45862.

[40] M. H. A. Kudus *et al.*, "Nonisothermal Kinetic Degradation of Hybrid CNT/Alumina Epoxy Nanocomposites," *Metals*, vol. 11, no. 4, p. 657, Apr. 2021, doi: 10.3390/met11040657.
[41] L. Li, C. Guan, A. Zhang, D. Chen, and Z. Qing, "Thermal stabilities and the thermal degradation kinetics of polyimides," *Polym. Degrad. Stab.*, vol. 84, no. 3, pp. 369–373, Jun. 2004, doi: 10.1016/j.polymdegradstab.2003.11.007.
[42] F. Ali, S. Saeed, S. S. Shah, and L. Duclaux, "Synthesis, kinetics and thermal stability of napthalenic polyimide silica nanocomposites," *Mater. Res. Express*, vol. 6, no. 2, p. 025052, Nov. 2018, doi: 10.1088/2053-1591/aaf1d7.
[43] S. Yousef, J. Eimontas, N. Striūgas, S. P. Subadra, and M. A. Abdelnaby, "Thermal degradation and pyrolysis kinetic behaviour of glass fibre-reinforced thermoplastic resin by TG-FTIR, Py-GC/MS, linear and nonlinear isoconversional models," *J. Mater. Res. Technol.*, vol. 15, pp. 5360–5374, Nov. 2021, doi: 10.1016/j.jmrt.2021.11.011.
[44] D. Bridges, R. Xu, and A. Hu, "Microstructure and mechanical properties of Ni nanoparticle-bonded Inconel 718," *Mater. Des.*, vol. 174, p. 107784, Jul. 2019, doi: 10.1016/j.matdes.2019.107784.
[45] W. Yang *et al.*, "Influence of Heating Rate on the Structure and Mechanical Properties of Aromatic BPDA–PDA Polyimide Fiber," *Polymers*, vol. 12, no. 3, p. 510, Feb. 2020, doi: 10.3390/polym12030510.
[46] M. B. H. Othman, H. Md Akil, S. Z. Md Rasib, A. Khan, and Z. Ahmad, "Thermal properties and kinetic investigation of chitosan-PMAA based dual-responsive hydrogels," *Ind. Crops Prod.*, vol. 66, pp. 178–187, Apr. 2015, doi: 10.1016/j.indcrop.2014.12.057.
[47] S. Xu, D. Lin, R. Li, J. Zhan, G. Tian, and D. Wu, "Effect of chemical structures and environmental factors on the thermal degradation mechanism of polyimide: Experiments and molecular dynamics simulations," *Mater. Today Chem.*, vol. 40, p. 102242, Sep. 2024, doi: 10.1016/j.mtchem.2024.102242.